

# SynthSeg: Domain Randomisation for Segmentation of Brain MRI Scans of any Contrast and Resolution

Benjamin Billot<sup>1</sup>, Douglas N. Greve<sup>2</sup>, Oula Puonti<sup>3</sup>, Axel Thielscher<sup>3,4</sup>, Koen Van Leemput<sup>2,4</sup>, Bruce Fischl<sup>2,5,6</sup>, Adrian V. Dalca<sup>2,5</sup>, and Juan Eugenio Iglesias<sup>1,2,5</sup>, for the ADNI\*

**Abstract**—Despite advances in data augmentation and transfer learning, convolutional neural networks (CNNs) have difficulties generalising to unseen target domains. When applied to segmentation of brain MRI scans, CNNs are highly sensitive to changes in resolution and contrast: even within the same MR modality, decreases in performance can be observed across datasets. We introduce SynthSeg, the first segmentation CNN agnostic to brain MRI scans of any contrast and resolution. SynthSeg is trained with synthetic data sampled from a generative model inspired by Bayesian segmentation. Crucially, we adopt a *domain randomisation* strategy where we fully randomise the generation parameters to maximise the variability of the training data. Consequently, SynthSeg can segment preprocessed and unprocessed real scans of any target domain, without retraining or fine-tuning. Because SynthSeg only requires segmentations to be trained (no images), it can learn from label maps obtained automatically from existing datasets of different populations (e.g., with atrophy and lesions), thus achieving robustness to a wide range of morphological variability. We demonstrate SynthSeg on 5,500 scans of 6 modalities and 10 resolutions, where it exhibits unparalleled generalisation compared to supervised CNNs, test time adaptation, and Bayesian segmentation. The code and trained model are available at [github.com/BBillot/SynthSeg](https://github.com/BBillot/SynthSeg).

**Index Terms**—Domain randomisation, contrast and resolution invariance, segmentation, CNN, neuroimaging.

## 1 INTRODUCTION

### 1.1 Motivation

SEGMENTATION of brain MRI scans is of paramount importance in neuroimaging, as it enables volumetric and shape analyses that are frequently used to characterise brain morphology in healthy and diseased populations [1]. Although manual delineation is considered the gold standard in segmentation, this procedure is extremely tedious and costly, which prevents the analysis of large datasets. Moreover, segmentation of brain scans requires expertise in neuroanatomy, which, even if available, suffers from severe inter- and intra-rater reproducibility issues [2]. For these reasons, automated segmentation methods have been proposed as an alternative fast and reproducible solution.

Automated segmentation strategies, which currently rely mostly on supervised convolutional neural networks (CNNs) [3], [4], [5], are widespread in research applications, where they are a prerequisite in numerous analyses such

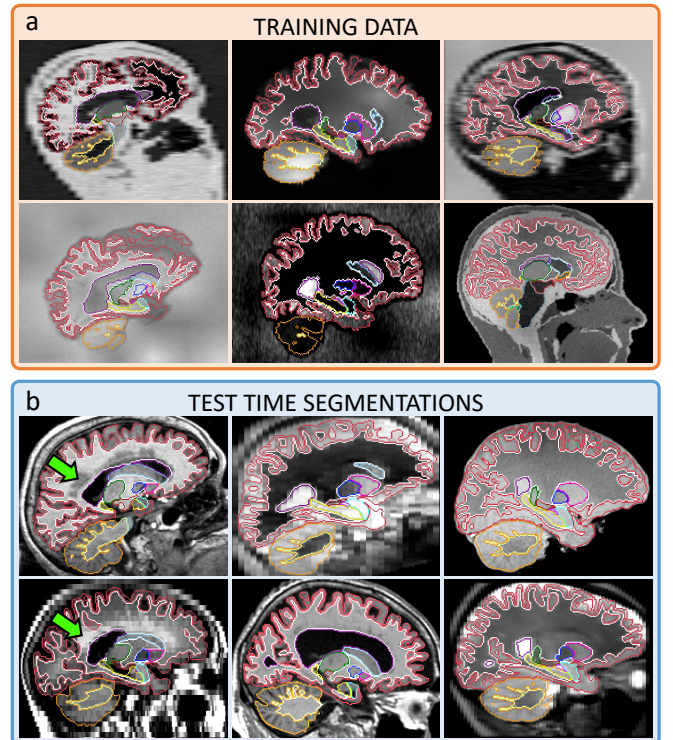


Fig. 1. (a) Examples of synthetic 3D scans used to train SynthSeg and contours of the corresponding ground truth. (b) Test time segmentations for a variety of modalities and resolutions, on subjects spanning a wide age range, some presenting large atrophy patterns and white matter lesions (green arrows). We emphasise that these segmentations are obtained with the same network, without retraining or fine-tuning.

<sup>1</sup>Centre for Medical Image Computing, University College London, UK

<sup>2</sup>Martinos Center for Biomedical Imaging, Department of Radiology, Massachusetts General Hospital and Harvard Medical School, USA

<sup>3</sup>Danish Research Centre for Magnetic Resonance, Centre for Functional and Diagnostic Imaging and Research, Copenhagen University Hospital Amager and Hvidovre, Denmark

<sup>4</sup>Department of Health Technology, Technical University of Denmark

<sup>5</sup>Computer Science and Artificial Intelligence Laboratory, Massachusetts Institute of Technology, USA

<sup>6</sup>Program in Health Sciences and Technology, Massachusetts Institute of Technology, USA

\*Data used in preparation of this article were obtained from the Alzheimer's Disease Neuroimaging Initiative (ADNI) database (<http://adni.loni.usc.edu>). The investigators within the ADNI contributed to the design and implementation of ADNI and/or provided data but did not participate in analysis of this report. A complete listing of ADNI investigators at: [adni.loni.usc.edu/wp-content/uploads/how\\_to\\_apply/ADNI\\_Acknowledgement\\_List.pdf](http://adni.loni.usc.edu/wp-content/uploads/how_to_apply/ADNI_Acknowledgement_List.pdf)

as volumetry, morphology and connectivity studies [6]. The development of segmentation methods in research has been driven by the abundance of high quality scans as well as the inclusion in most imaging protocols of a 3D MP-RAGE sequence [7] at 1 mm isotropic resolution with very good contrast between white and grey matter.

In comparison, scans acquired in the clinic for diagnostic purposes present a much higher variability in acquisition procedures. Rather than 3D isotropic volumes, physicians prefer scans with fewer slices acquired in 2D, which can be efficiently inspected under time constraints. This leads to a huge variability in terms of image orientations (axial, coronal, or sagittal) and resolutions (in-plane resolution, and slice spacing). Moreover, such 2D acquisitions often use a large slice thickness to increase signal-to-noise ratios, which also introduces important partial voluming (PV). This PV effect arises when several tissue types are mixed within the same voxel, resulting in an averaged intensity that is not necessarily representative of the underlying tissues [8], which often causes automated segmentation methods to underperform [9]. In addition to resolution changes, imaging protocols span a huge diversity in sequences and MR modalities, each aiming at investigating specific tissue properties, and the resulting variations in intensity distributions have been shown to substantially decrease the accuracy of modern supervised strategies.

The lack of tools that are able to cope with the large variability in MR contrast and resolution hinders the adoption of quantitative morphometry in the clinic. Moreover, it precludes the analysis of vast amounts of retrospective clinical scans, which are left unexplored in picture archiving and communication systems (PACS) in hospitals around the world. Therefore, there is a clear need for fast, accurate and reproducible automated segmentation methods, which can adapt to a wide range of subject populations, and are robust against changes in MR contrast and resolution.

## 1.2 Improving the generalisation of neural networks

Modern image processing mostly relies on deep neural networks, which yield state-of-the-art results in many computer vision tasks such as semantic image segmentation [10], [11], classification [12], [13], object detection [14], [15], super-resolution [16], [17], and image generation [18], [19]. Nevertheless, deep learning networks are also known for their lack of generalisation to domains different from the training data, an issue known as “domain-gap” or “distribution shift” [20], [21]. Indeed, the accuracy of neural networks is likely to decrease considerably when tested on unseen datasets, even if they represent the same type of scenes or objects [22]. As mentioned above, the domain gap is particularly problematic in brain MRI segmentation, where networks have been shown not to generalise well across different modalities or resolutions [23], [24].

The robustness of neural networks is often improved with data augmentation techniques. These approaches usually include random spatial deformation (affine and elastic transformations, cropping, flipping), as well as changes in intensity distributions [25], [26]. However, the parameters used for such operations are often handcrafted, and thus suboptimal. Instead, recent methods optimise the augmentation directly during training [27], [28]. Interestingly, these

techniques often result in highly aggressive data augmentation that goes beyond realistic shapes and intensity distributions, hence agreeing with other empirical results in the literature that very strong augmentation is beneficial [29], [30], [31]. Rather than directly transforming the available data, other recent augmentation strategies have also explored the use of Generative Adversarial Networks to synthetically increase the size of the training dataset [32], [33]. While data augmentation increases the robustness of neural networks by densifying and, to some extent, enlarging the scope of their training data, it generally remains insufficient to bridge the domain gap on its own.

The lack of generalisation of deep learning methods has sparked a vivid interest in transfer learning approaches, which explicitly seek to generalise to given target domains. A standard approach is to pre-train a network on a source domain with data labelled for a related task, and then fine-tune it on a target domain with typically much less available training examples [21], [34]. This strategy has been widely applied, and yields good results in many different applications [35], [36]. Another solution consists in mapping the source and target domains to a common latent space, where a classifier can be trained [37], [38]. Rather than aligning different domains in feature space, generative domain adaptation has sought to match them directly in pixel space with “image-to-image” translation methods [39], [40]. However, these approaches are not designed for specific downstream applications, and may exhibit semantic inconsistencies [41]. Therefore, recent strategies have proposed to combine the loss of the end task with the loss of the image translation model for improved semantic matching [41], [42].

Although domain adaptation techniques can bridge the domain gap, they often require a considerable amount of supervised data for training (both in the source and target domains). For this reason, there is significant interest in replacing real datasets with realistic images produced by graphics engines [43], [44], possibly from video games [45]. In addition to providing a realistic and safe environment to test systems before real-world deployment [46], this strategy enables the use of huge training datasets with ground truth obtained by construction rather than human annotation. While generated images may look remarkably realistic, the domain shift problem (here known as “reality gap” [20]) still persists, and in practice, synthetic datasets are mostly used to pre-train networks in domain adaptation or other transfer learning schemes [45], [47]. However, recent approaches have shown competitive results with synthetic training data alone, by optimising the generation process to reduce the reality gap, for example with adversarial networks [48] or by computing a semantic loss on a downstream task [49]. Overall, while all the aforementioned methods enable a boost in performance for a specific domain, they still require retraining or fine-tuning for every new target distribution, and thus do not resolve the general lack of generalisation of deep neural networks on unseen domains.

Meanwhile, descriptive generative models (i.e., based on descriptive sets of rules) have recently regained interest. Unlike learning-based generation methods, these models offer full control over the generation process. Hence, instead of training them to match a specific domain (which would inevitably fall back to the reality gap), one can considerably

enlarge the distribution of the synthetic images by *fully randomising* the generation parameters (colour, shape, etc.). This new learning strategy is known as Domain Randomisation, and is motivated, as mentioned above, by converging evidence that unrealistic augmentation can improve generalisation [27], [29], [31]. If pushed to the extreme, this approach yields highly unrealistic samples, in which case real images are encompassed within the landscape of the synthesised training data [50], [51]. As a result, domain randomisation seeks to bridge all domain gaps of interest in a given semantic space (e.g., street views, brain scans), rather than solving this problem for each domain gap separately.

### 1.3 Contrast and resolution invariance in segmentation of brain MRI scans

Traditionally, atlas-based approaches have prevailed in automated methods for brain MRI segmentation. In this paradigm, the simplest strategy is to deform a single atlas (i.e., a labelled 3D image) to a test scan with an image registration algorithm [52], and use the deformed labels as the estimated segmentation [53]. In order to increase the anatomical variability covered by the model, this approach can be extended to multi-atlas segmentation (MAS) [54], where several atlases are registered to the test scan, which is segmented by merging all the warped label maps with a label fusion strategy [55], [56]. While MAS was originally intended for intra-modality segmentation, it can be adapted to cross-modality problems [57] by employing cross-modality registration metrics (e.g., mutual information) [58]. Nevertheless, the accuracy of MAS highly depends on the quality of the registrations, which are often inaccurate in cross-modality scenarios [59]. Moreover, MAS is computationally expensive due to the numerous registrations required for each new test scan [56]. Although this issue is being ameliorated by the recent advances in fast CNN-based registration [60], the ability of such methods to handle arbitrary MRI contrasts is yet to be demonstrated.

Contrast-invariance in segmentation of brain MRI scans has traditionally been addressed with Bayesian segmentation. This approach is based on a generative model, which combines an anatomical prior and an intensity likelihood distribution. The former is often represented by a statistical atlas, and the latter models the intensities of different brain tissues, typically with a Gaussian Mixture Model (GMM). Scans are then segmented by “inverting” this forward model with Bayesian inference. Robustness to MR contrasts is achieved by a subclass of Bayesian methods with unsupervised likelihood models, where the GMM parameters are estimated from each test scan separately [61], [62]. These unsupervised methods are very popular in neuroimaging, as they can segment scans of any contrast, even with high resolution (HR) atlases built from *ex vivo* acquisitions [63].

Although Bayesian segmentation is substantially faster than MAS, it still requires important time resources (approximately 12 minutes per scan), which hinders its scalability to large datasets and deployment for time-sensitive applications. Additionally, the accuracy of Bayesian segmentation methods is limited by changes in resolution, as they are sensitive to PV [8]. The Bayesian framework can easily model scans at a specific low resolution (LR) with PV by appending

smoothing and downsampling steps to the standard HR forward model [9]. However, inferring HR segmentations from LR scans quickly becomes intractable, as it requires marginalising over all possible configurations of HR labels within each LR supervoxel. While simplifications can be made in simple cases (e.g., uni-modality scans with few label classes) [9], [64], PV-aware Bayesian segmentation may still be unfeasible for other cases, especially multi-modality images with channels of different resolutions.

Modern medical image segmentation mostly relies on CNNs [4], [5], and particularly fully convolutional networks [10], best represented by the UNet architecture [3], [65], [31], [66]. While these networks obtain fast and accurate segmentations on their training domains, they typically do not generalise well to unseen contrasts [67], [65] and resolutions [24], [68]. For this reason, such learning methods need to be retrained for any new combination of contrast and resolution, often requiring new labelled data. Thus, supervised CNNs are not widespread in the main neuroimaging packages (e.g., SPM [62], FreeSurfer [69], FSL [70]).

Different methods have been proposed to improve the ability of CNNs to generalise to different contrasts. First, aggressive augmentation strategies [28], [31] have been shown to considerably improve the robustness of CNNs, albeit not being able to generalise to different modalities. Another approach is to train a network on multi-modality scans by applying modality dropout, which results in a network able to individually segment all training modalities [71]. Despite increasing the robustness of segmentation networks, these methods perform poorly on MR modalities unseen during training, and thus require labelled training data for all target modalities. Other methods rely on introducing synthetic contrasts variations that are not initially available, in order to augment the training data [65], [72]. More generally, cross-modality segmentation has been addressed by an array of transfer learning strategies [73], [74], including unsupervised domain adaptation [75], [5], [76], and test time adaptation [77], [78]. In previous work, we have proposed to build contrast-adaptiveness by employing a CNN to solve the inference problem within the Bayesian framework [79]. These approaches alleviate the need for supervised data, but they still need to be retrained (in the case of unsupervised domain adaptation) or fine-tuned (test time adaptation, CNN-based Bayesian segmentation) to each target domain. To the best of our knowledge, no deep-learning based method has been proposed to readily segment brain MRI scans of any contrast with a single model.

Meanwhile, very few solutions have been proposed to make CNNs robust against changes in resolution. Transfer learning approaches have been shown to learn to segment scans at a specific resolution given appropriate training data [23], [68]. However, to the best of our knowledge, no attempt has been made to segment brain MRI scans of arbitrary resolution with CNNs.

### 1.4 Contribution

In this paper, we present SynthSeg, the first neural network to readily segment brain MRI scans of *any* contrast and resolution, without having to be retrained or fine-tuned (Figure 1). This work extends two of our recent articles

about contrast-adaptiveness [80] and PV simulation [81] for segmentation of brain MRI scans. Here we substantially expand these works by building, for the first time, robustness to brain scans of any resolution (in addition to contrast-invariance), as well as adaptiveness to a wide range of subject populations. All aspects of the presented method are thoroughly evaluated in four new experiments.

Specifically, SynthSeg is a CNN trained with synthetic scans obtained by leveraging a generative model inspired from the Bayesian segmentation framework, with fully randomised parameters including aggressive augmentation and artefacts modelling. Crucially, the synthetic scans are sampled on the fly, which exposes the network to a different contrast, orientation, and resolution at each mini-batch, and thus forces it to learn features agnostic to these variables. Furthermore, we apply a random subset of common pre-processing operations (e.g., skull stripping and bias field correction) to each training example, such that the network can segment scans with or without preprocessing.

By adopting this domain randomisation strategy, the presented method only needs to be trained once. This is a considerable improvement over traditional supervised CNNs and domain adaptation strategies, which all need retraining or fine-tuning for each new combination of contrast and resolution. Moreover, training SynthSeg is greatly facilitated by the fact that it only requires a set of anatomical segmentations: training images are built from these label maps, which also eliminates manual delineations mistakes, since the synthetic scans are perfectly aligned with their segmentations by construction.

Overall, SynthSeg almost yields the level of accuracy of supervised networks tested on their training domain. Importantly, SynthSeg exhibits outstanding generalisation ability, and consistently outperforms state-of-the-art domain adaptation strategies, particularly for large domain gaps (e.g., with modalities and resolutions different from the source domain). Finally, SynthSeg also outperforms Bayesian segmentation tools (especially for clinical scans with PV), while running considerably faster.

## 2 METHODS

### 2.1 Generative model

SynthSeg relies on a generative model of brain MRI from which we sample synthetic scans to train a segmentation network [80], [81], [82]. Crucially, the training images are sampled on the fly with fully randomised parameters, such that the network is exposed to a different combination of contrast, resolution, morphology, artefacts, and noise at each mini-batch (Figure 2). In this section, we describe the generative model, which is exemplified in Figure 3.

#### 2.1.1 Label map selection and spatial augmentation

The proposed generative model assumes the availability of  $N$  high resolution (HR) training label maps (i.e., segmentation maps)  $S = \{S_n\}_{n=1}^N$  defined over discrete spatial coordinates  $(x, y, z)$ . Let all segmentations take their values from a set of  $K$  labels, i.e.,  $S_n(x, y, z) \in \{1, \dots, K\}$ , where each label corresponds to a cerebral or extra-cerebral anatomical structure. We emphasise that we do not put a

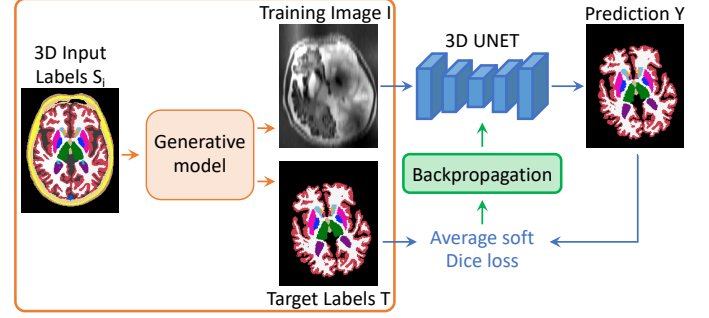


Fig. 2. Overview of a training step. At each mini-batch, we randomly select a 3D label map and sample a training pair  $\{I, T\}$  from the generative model. The obtained image is then run through the network, and its prediction  $Y$  is used to compute the average soft Dice loss, that is backpropagated to update the weights of the network.

condition on how these training label maps were generated (i.e., manually, automatically, or a combinations thereof).

The generative process starts by randomly selecting a segmentation  $S_i$  from the training dataset (Figure 3a). In order to increase the variability of the available segmentations, we deform the selected label map into  $L$  with a random spatial transform  $\phi$ , which is the composition of an affine transformation  $\phi_{\text{aff}}$  and a non-linear deformation  $\phi_{\text{nonlin}}$ .

We form the affine transformation  $\phi_{\text{aff}}$  by composing three rotations  $(\theta_x, \theta_y, \theta_z)$ , three scalings  $(s_x, s_y, s_z)$ , three shearings  $(sh_x, sh_y, sh_z)$ , and three translations  $(t_x, t_y, t_z)$  along the  $x, y$  and  $z$  axes. These 12 parameters are independently sampled from continuous uniform distributions:

$$\begin{aligned} \theta_x, \theta_y, \theta_z &\sim \mathcal{U}(a_{\text{rot}}, b_{\text{rot}}), \\ s_x, s_y, s_z &\sim \mathcal{U}(a_{\text{sc}}, b_{\text{sc}}), \\ sh_x, sh_y, sh_z &\sim \mathcal{U}(a_{\text{sh}}, b_{\text{sh}}), \\ t_x, t_y, t_z &\sim \mathcal{U}(a_{\text{tr}}, b_{\text{tr}}), \\ \phi_{\text{aff}} &= \text{Affine}(\theta_x, \theta_y, \theta_z, s_x, s_y, s_z, sh_x, sh_y, sh_z, t_x, t_y, t_z), \end{aligned}$$

where  $a_{\text{rot}}, b_{\text{rot}}, a_{\text{sc}}, b_{\text{sc}}, a_{\text{sh}}, b_{\text{sh}}, a_{\text{tr}}, b_{\text{tr}}$  are the predefined minimum and maximum values of the uniform distributions, and  $\text{Affine}(\cdot)$  refers to the composition of the transforms corresponding to the aforementioned parameters.

The non-linear component is a diffeomorphic transform obtained as follows. First, we sample a small grid of size  $10 \times 10 \times 10 \times 3$  from a zero-mean Gaussian distribution of standard deviation  $\sigma_{\text{SVF}}$ , which is drawn from a uniform distribution  $\mathcal{U}(0, b_{\text{nonlin}})$ . This tensor is then upsampled to full image size with a trilinear interpolation, such that we obtain a smooth stationary velocity field (SVF) on the grid of  $L$ . Finally, we compute the Lie exponential of the resulting SVF by integrating it with a scale-and-square approach [83], to produce a smooth and invertible diffeomorphic field:

$$\begin{aligned} \sigma_{\text{SVF}} &\sim \mathcal{U}(0, b_{\text{nonlin}}), \\ \text{SVF}' &\sim \mathcal{N}_{10 \times 10 \times 10 \times 3}(0, \sigma_{\text{SVF}}), \\ \text{SVF} &= \text{Upscale}(\text{SVF}'), \\ \phi_{\text{nonlin}} &= \exp(\text{SVF}). \end{aligned}$$

Finally, the spatially augmented segmentation map  $L$  is obtained by applying the deformation  $\phi$  to the selected label map  $S_i$  using nearest neighbour interpolation (Figure 3b):

$$L = S_i \circ \phi = S_i \circ (\phi_{\text{aff}} \circ \phi_{\text{nonlin}}). \quad (1)$$



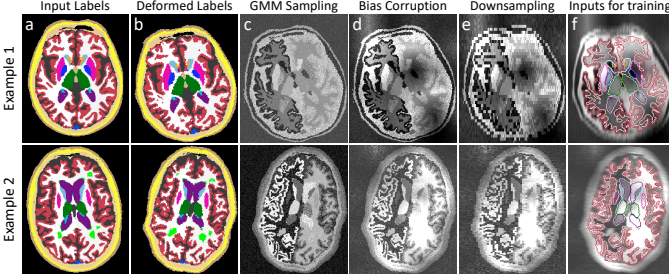


Fig. 3. Intermediate steps of the generative model: (a) we first randomly select an input label map, that is (b) spatially augmented with a 3D transformation. (c) A first synthetic image is obtained by sampling a GMM of randomised parameters at HR. (d) The result is then corrupted with a bias field and further intensity augmentation. (e) Slice spacing and thickness are simulated by successively blurring and downsampling at random LR. (f) The training inputs are obtained by resampling to HR, and keeping the labels of the relevant structures (at the original resolution) for segmentation.

### 2.1.2 First HR synthetic image

Once the input segmentation has been deformed, we generate a first synthetic scan  $G$  at HR by sampling a GMM conditioned on  $L$  (Figure 3c). Specifically, the GMM comprises as many components as the number of anatomical labels  $K$ , and is possibly multivariate to synthesise images with  $C$  input channels ( $C \geq 1$ ), where we assume the covariances between channels to be zero. For convenience, we regroup all the means and standard deviations governing the GMM in  $M_G = \{\mu_{k,c}\}_{1 \leq k \leq K, 1 \leq c \leq C}$ , and  $\Sigma_G = \{\sigma_{k,c}\}_{1 \leq k \leq K, 1 \leq c \leq C}$  respectively. Crucially, in order to randomise the contrast of the generated scans, all the parameters in  $M_G$  and  $\Sigma_G$  are sampled at each mini-batch from the respective uniform distributions of range  $\{a_\mu, b_\mu\}$  and  $\{a_\sigma, b_\sigma\}$ . All the components of the GMM share the same prior distribution, to avoid a bias towards any specific contrast. We highlight that  $\Sigma_G$  enables us to jointly model tissue heterogeneities, and approximate scanner thermal noise (usually represented as a Rice distribution [84]). Therefore,  $a_\sigma^2$  is taken as the variance of the background thermal noise. The intensities of a channel  $G_c$  of  $G$  are then given by independently sampling at each spatial location  $(x, y, z)$  the Gaussian distribution indexed by the label  $L(x, y, z)$ :

$$\begin{aligned} \mu_{k,c} &\sim \mathcal{U}(a_\mu, b_\mu), \\ \sigma_{k,c} &\sim \mathcal{U}(a_\sigma, b_\sigma), \\ G_c(x, y, z) &\sim \mathcal{N}(\mu_{L(x,y,z),c}, \sigma_{L(x,y,z),c}^2). \end{aligned} \quad (2)$$

### 2.1.3 Bias field and intensity augmentation

We then apply bias field and intensity augmentation steps to further enlarge the intensity distribution of the synthetic scans and make SynthSeg robust to common artefacts. We start by modelling non-uniformities in the sensitivity profiles of the scanner receive coils, which translate into a smoothly varying, multiplicative “bias field” [85]. The strategy employed here is similar to the one used for synthesising non-linear deformations in 2.1.1, and is repeated independently for each channel. Specifically, we create a small LR field of shape  $4 \times 4 \times 4$  by sampling a zero-mean Gaussian distribution, with a standard deviation  $\sigma_{B,c}$  drawn from a uniform distribution  $\mathcal{U}(0, b_B)$ . We then upsample this small

grid to the size of  $G$ , and take the voxel-wise exponential to ensure the non-negativity of the field. Finally, we obtain a biased image  $G^B$  by multiplying the resulting field  $B$  and  $G$  (Figure 3d):

$$\begin{aligned} \sigma_{B,c} &\sim \mathcal{U}(0, b_B), \\ B'_c &\sim \mathcal{N}_{4 \times 4 \times 4}(0, \sigma_{B,c}^2), \\ B_c &= \text{Upsample}(B'_c), \\ G_c^B(x, y, z) &= G_c(x, y, z) \times \exp[B_c(x, y, z)]. \end{aligned} \quad (3)$$

A final HR image  $I^{HR}$  is produced by normalising the channels of  $G^B$  between 0 and 1 with min-max normalisation, and applying a different Gamma transform (voxel-wise exponentiation) to each channel. The exponent of the Gamma augmentation is sampled in the logarithmic domain by drawing from a zero-mean Gaussian distribution of standard deviation  $\sigma_\gamma$ . This transform enables to skew the distribution while leaving intensities in the  $[0, 1]$  interval. As a result, every channel  $I_c^{HR}$  of  $I^{HR}$  is given by:

$$\begin{aligned} \gamma_c &\sim \mathcal{N}(0, \sigma_\gamma^2), \\ I_c^{HR}(x, y, z) &= \left( \frac{G_c(x, y, z) - \min_{x,y,z} G_c}{\max_{x,y,z} G_c - \min_{x,y,z} G_c} \right)^{\exp(\gamma_c)}. \end{aligned} \quad (4)$$

### 2.1.4 Simulation of resolution variability

In order to make the network agnostic to resolution and robust to PV effects, we model differences in acquisition direction (i.e., axial, coronal, sagittal), slice spacing, and slice thickness. First, we randomly select an orientation for each channel. Then, we independently sample their associated slice spacing  $r_c$  from  $\mathcal{U}(r_{targ}, b_{res})$ , where  $r_{targ}$  represents the isotropic resolution of the training label maps (typically  $1 \text{ mm}^3$ ), which will be used as the target resolution for segmentation. While slice spacing and thickness are often equal for thin slices, this is not always the case for clinical scans of lower resolution, where thickness seeks to find a balance between higher signal-to-noise ratio (i.e., thicker slices) and slice crispness (i.e., thinner slices with less signal from out-of-plane tissues). Therefore, we independently sample the slice thickness  $r_c^{thick}$  of each channel in  $\mathcal{U}(r_{targ}, r_c)$ , which we bound by  $r_c$  since slices very rarely overlap in practice. Note that  $r_c$  and  $r_c^{thick}$  are  $1 \times 3$  vectors.

We then simulate slice thickness by blurring  $I_c^{HR}$  into  $I_c^\sigma$  with a kernel representing the MRI slice excitation profile. These profiles are difficult to model accurately, as they are designed with numerical optimisation methods (e.g., the Shinnar-Le Roux algorithm [86]). Instead, we replace them with simpler Gaussian kernels with standard deviation  $\sigma_c^{thick}$ , such that the power of the HR signal is divided by 10 at the cut-off frequency [81]. Moreover, we multiply  $\sigma_c^{thick}$  by a random coefficient  $\alpha$  (sampled from a distribution  $\mathcal{U}(a_\alpha, b_\alpha)$  centred around 1). This enables us to introduce small deviations from the nominal thickness, and to mitigate the Gaussian assumption, which is also ameliorated by the wide range of simulated thicknesses across mini-batches.

After blurring the image, slice spacing is modelled by downsampling each channel  $I_c^\sigma$  (still defined on the HR grid) to the prescribed low resolution  $r_c$  with trilinear interpolation (Figure 3e). This process yields a set of  $C$  channels  $I_c^{LR}$ , each defined on its own LR space. Finally, we independently upsample each LR channel back to the

original HR space with linear interpolation. This last step mimics the preprocessing at test time, when input images will be resampled to the target isotropic resolution  $r_{targ}$ , such that the CNN produces crisp segmentations on the HR grid regardless of the native resolution of the inputs. This process can be summarised as:

$$\begin{aligned}
 \mathbf{r}_c &\sim \mathcal{U}(r_{targ}, b_{res}), \\
 \mathbf{r}_c^{thick} &\sim \mathcal{U}(r_{targ}, \mathbf{r}_c), \\
 \alpha &\sim \mathcal{U}(a_\alpha, b_\alpha), \\
 \sigma_c^{thick} &= 2\alpha \log(10)(2\pi)^{-1} \mathbf{r}_c^{thick} / r_{targ}, \\
 I_c^\sigma &= I_c^{HR} * \mathcal{N}[0, \text{diag}(\sigma_c^{thick})], \\
 I_c^{LR} &= \text{Resample}(I_c^\sigma; \mathbf{r}_c), \\
 I_c &= \text{Resample}(I_c^{LR}; r_{targ}). \tag{5}
 \end{aligned}$$

### 2.1.5 Model outputs

The generative model is completed by resetting a fixed subset of the labels in  $L$  to the background value. While synthesising some structures is critical during training (e.g., the extra-cerebral regions), segmenting them may be of little interest. As a result, the output of this generative model at each mini-batch is a pair  $\{I, T\}$  at high resolution  $r_{targ}$ , where  $I$  has  $C$  channels  $I = \{I_c\}_{1 \leq c \leq C}$ , and  $T$  is the target segmentation with  $K'$  labels, with  $K' \leq K$  (Figure 3f).

## 2.2 Segmentation network and learning

Given a set of label maps, we use the proposed generative model to form pairs  $\{I, T\}$  that are used to train a segmentation network on the fly in a supervised fashion. In this study we employ a 3D UNet architecture [3] that we have used in previous works with synthetic MRI scans [80], [81], [87]. Specifically, the network consists of 5 levels, each separated with a batch-normalisation layer [88] along with a max-pooling (contracting path), or upsampling operation (expanding path). All levels comprise 2 convolution layers, each employing  $3 \times 3 \times 3$  kernels. Every convolutional layer is associated with an Exponential Linear Unit activation function [89], except for the last one, which uses a softmax function. The first layer contains 24 feature maps, and this number is doubled after each max-pooling, and halved after each upsampling. Following the UNet architecture, we use skip connections between corresponding levels across the contracting and expanding paths. Note that we adopt a UNet architecture as it is the most widely used in medical image segmentation [3], [65], [31], but the network architecture is not a focus of this work, and it could be replaced with any other segmentation network.

During training, the weights of the networks are optimised with the average soft Dice loss [4] between the ground truth segmentation  $T$  and the predicted output  $Y$ . If  $Y_k = \{Y_k(x, y, z)\}$  designates the predicted probability map for label  $k$  ( $k \in \{1, \dots, K'\}$ ), and  $T_k = \{T_k(x, y, z)\}$  is the ground truth for the same label in one-hot encoding, the loss function can be expressed as:

$$\text{Loss}(Y, T) = 1 - \sum_{k=1}^{K'} \frac{2 \times \sum_{x,y,z} Y_k(x, y, z) T_k(x, y, z)}{\sum_{x,y,z} Y_k(x, y, z)^2 + T_k(x, y, z)^2}. \tag{6}$$

The network is trained using the Adam optimiser [90] for 300,000 steps (largely sufficient for all models to converge) with a learning rate of  $10^{-4}$ , and a batch-size of 1. The network is trained twice, and the weights are saved every 10,000 steps. The retained model is then selected relatively to a validation set, even though there is no perceptible change in validation scores after convergence of the learning curve. In practice, the generative model and the segmentation network are concatenated in a single model, which is entirely implemented on the GPU in Keras [91] with a Tensorflow backend [92]. In total, training takes approximately seven days on a Nvidia Quadro RTX 6000 GPU.

## 2.3 Inference

At test time, a light data preparation is performed to adjust test scans to the format of the training data. Specifically, the inputs are resampled to high resolution  $r_t$ , and their intensity distributions are rescaled between 0 and 1 with robust min-max normalisation (using the 1<sup>st</sup> and 99<sup>th</sup> percentiles as minimum and maximum values). The preprocessed scans are then fed to the network (stripped of the generative model) to obtain predicted probabilistic maps for each label. In practice, we also perform test-time augmentation, where we predict the segmentations of the test images as well as a right-left flipped version of them. The posteriors of the flipped inputs are then reverted and averaged with the predictions in native space. In addition to ensuring lateral invariance, this process slightly improved segmentation accuracy in our early experiments.

The predictions are automatically postprocessed with the following steps. Based on *a priori* anatomical knowledge, we first regroup the  $K'$  predicted labels into topological classes. For each class we successively: (i) sum all the posteriors corresponding to the labels of this class, (ii) obtain a mask for this class by thresholding the result by a low value (arbitrarily set to 0.1), (iii) keep the biggest connected component, and (iv) individually apply the obtained mask to the posteriors of all the labels for this class. Overall, this operation leads to a slight increase in the quality of the predictions by performing a topologically enhanced version of biggest connected component. In the end, the final segmentations are obtained by performing an argmax operation on the masked posteriors.

In total, segmenting a test scan takes around 6 seconds on a Nvidia Titan XP GPU (12GB), including the data preparation, prediction, and postprocessing steps.

## 2.4 Generative model hyperparameters

The central contribution of this work resides in the domain randomisation strategy that we employ to greatly increase the variability of the generated scans, in order to build a model agnostic to any target domain in the semantic space of brain images. Therefore, we sample all model parameters from flat uninformative uniform priors, such that the training examples yield a visual aspect that goes far beyond realistic appearance in terms of intensity distribution, shape and artefacts. The values of the hyperparameters controlling these priors are grouped in Supplement 1. In practice, these values were obtained by further increasing the range of distributions used in our previous works [80], [81], which were set by visual inspection of the generated images.

### 3 GENERAL EXPERIMENTAL SETUP

#### 3.1 MRI data

In total, our experiments employ 8 datasets, comprising 5,500 scans of 6 different modalities and 10 resolutions, which we describe in this section. All subject information is summarised in Table 1, which also presents the split between training, validation, and testing sets.

**T1-39:** This first dataset consists of 39 unpreprocessed T1-weighted (T1) scans available with manual labels for 30 cerebral structures [93]. They were acquired with an MP-RAGE sequence at 1 mm isotropic resolution, and are split between training (20), validation (4), and testing (15). We emphasise that we only use the label maps to train SynthSeg.

**HCP:** This second dataset contains 600 unpreprocessed T1 scans of young and healthy subjects (aged between 22 and 40 years old) from the Human Connectome Project [94]. Although the data was originally acquired at 0.7 mm isotropic resolution, we resample it at 1 mm<sup>3</sup> to match the resolution of the T1-39 data. We randomly select 500 scans for training, while the remaining ones are held out for testing.

**ADNI:** 600 scans from the Alzheimer’s Disease Neuroimaging Initiative (ADNI<sup>1</sup>). All are T1 scans acquired at approximately 1 mm resolution using a wide array of scanners and protocols. In contrast to HCP scans, this dataset comprises ageing subjects (from 62 to 91 years old), some diagnosed with mild cognitive impairment (MCI) or Alzheimer’s Disease (AD). As such, many subjects present strong atrophy patterns and large white matter lesions associated with ageing and/or AD. Scans are randomly split between training (500) and held out testing (100).

**T1mix:** We use this heterogeneous T1 dataset to assess the robustness of SynthSeg to intra-modality variations in contrasts due to differences in acquisition protocols, and hardware. It contains 1,000 scans collected from seven public datasets: ABIDE [95], ADHD200 [96], GSP [97], HABS [98], MCIC [99], OASIS [100], and PPMI [101]. Again, all scans are unpreprocessed and at approximately 1 mm<sup>3</sup> resolution. This dataset is used for testing only.

**FSM:** This dataset enables evaluation on two new modalities: in addition to T1 images, it also contains T2-weighted (T2) scans for 18 subjects and a sequence typically used in deep brain stimulation (DBS) [102]. All scans are unpreprocessed and at 1 mm<sup>3</sup> resolution. The DBS acquisitions use an MP-RAGE sequence with parameters: TR = 3000 ms, TI = 406 ms, TE = 3.56 ms, flip angle = 8°. Subjects are randomly divided between validation (3) and testing (15).

**MSP:** We also add a dataset consisting of 8 subjects with T1 and proton density (PD) acquisitions at 1 mm resolution [103]. These scans were skull stripped prior to availability, and are manually delineated for the same labels as T1-39.

1. The ADNI was launched in 2003 by the National Institute on Ageing, the National Institute of Biomedical Imaging and Bioengineering, the Food and Drug Administration, private pharmaceutical companies and non-profit organisations, as a \$60 million, 5-year public-private partnership. The main goal of ADNI is to test whether MRI, positron emission tomography (PET), other biological markers, and clinical and neuropsychological assessment can be combined to analyse the progression of mild cognitive impairment (MCI) and early AD. Markers of early AD progression can aid to develop new treatments and monitor their effectiveness, and decrease the time and cost of clinical trials.

TABLE 1

Summary of the employed datasets. The 10 test resolutions are 1mm<sup>3</sup> and 3/5/7mm in either axial, coronal, or sagittal direction. SynthSeg is trained solely on label maps.

Dataset	Subjects	Modality	Resolution
Training			
T1-39	20	SynthSeg: Label maps Baselines: T1	1 mm <sup>3</sup>
HCP	500	SynthSeg: Label maps Baselines: T1	1 mm <sup>3</sup>
ADNI	500	SynthSeg: Label maps Baselines: T1	1 mm <sup>3</sup>
Validation			
T1-39	4	T1	all tested resolutions
FSM	3	T2, DBS	all tested resolutions
Testing			
T1-39	15	T1	all tested resolutions
HCP	100	T1	1 mm <sup>3</sup>
ADNI	100	T1	1 mm <sup>3</sup>
T1mix	1,000	T1	1 mm <sup>3</sup>
FSM	15	T1, T2, DBS	all tested resolutions
MSP	8	T1, PD	all tested resolutions
FLAIR	2,393	FLAIR	5 mm axial
CT	6	CT	3 mm axial

Despite its smaller size, this dataset enables evaluation on another contrast (PD) that is very different from T1.

**FLAIR:** This dataset comprises 2,393 fluid-attenuated inversion recovery (FLAIR) scans with at 1 × 1 × 5 mm resolution in axial direction. These subjects are from another separate subset of the ADNI database, and hence also present morphological patterns linked with ageing and AD. This dataset (used for testing only) assessment on LR images, which are representative of clinical applications.

**CT:** Finally, we assess the generalisation ability of SynthSeg to acquisitions different from MR, by testing it on computed tomography (CT) scans. Specifically, this dataset contains 6 images acquired at 1 × 1 × 3 mm in axial direction [104]. We underscore that CT scans are very challenging to segment due to their poor soft tissue contrast. Moreover, the subjects of this dataset all present small tumours, which alter the morphology of the brain, and thus increase the difficulty of the segmentation task.

In order to estimate the flexibility of SynthSeg against different resolutions, we artificially downsample all modalities from the T1-39, FSM, and MSP datasets (all at native 1 mm<sup>3</sup> resolution), to 9 different low resolutions: namely 3, 5 and 7 mm spacing in axial, coronal, and sagittal directions, with a slice thickness of 3, 4, and 4 mm respectively.

Except for the T1-39 and MSP datasets, no manual delineations are available for the rest of the scans. Hence, we process the T1 scans of the HCP, ADNI, T1mix, and FSM datasets with FreeSurfer in order to obtain segmentations that we use as silver standard ground truths. Similarly, we apply the same process to the FLAIR dataset and CT scans (where tumours are segmented as white matter), since they are available with corresponding 1 mm T1 acquisitions, that

we rigidly registered. However, we do not use the T1 images from these two datasets for testing since (i) we wish to reproduce clinical settings where isotropic T1 scans may not be available, and (ii) we already include a large amount of T1 scans in our experiments.

We highlight that, although employing such automated label maps may not be ideal for evaluation, FreeSurfer has been thoroughly demonstrated on numerous independent datasets for T1 scans [93], [105]. It also yields high Dice scores compared to manual segmentations for T1-39 (0.88, albeit biased by mixing FreeSurfer training and testing data) and MSp (0.85). Hence, it enables validation on large datasets, which would otherwise have been infeasible since manual tracings are extremely tedious and costly to obtain.

### 3.2 Training segmentations and population robustness

As indicated in Section 3.1, the training set comprises 20 label maps from T1-39, 500 from HCP, and 500 from ADNI. Mixing these label maps considerably increases the morphological variety of the synthetic scans (far beyond the capacity of the proposed spatial augmentation), and thus enlarges the robustness of SynthSeg to a wide range of populations.

We underscore that using automated label maps for training is possible because synthetic images are by design perfectly aligned with their segmentations. However, automated segmentations can present systematic biases (e.g., over-segmenting the hippocampus). For this reason, we add a prior on the selection of the input label maps, which are drawn with two-thirds chances from T1-39 (manual delineations), and one-third probability from either ADNI or HCP (automated labels).

To further increase the variability of the training label maps, we apply the following steps. First, we complete them with extra-cerebral labels obtained with a Bayesian segmentation approach [106], for which we only had access to the atlas (not to the delineations used for its construction [107]). Then, during training, one of the following options is randomly selected at each mini-batch: (i) keep all labels, (ii) suppress all extra-cerebral labels, or (iii) suppress all extra-cerebral labels except the CSF (Supplement 2). This process enables to simulate whole-head scans as well as (possibly imperfect) skull stripping. Moreover, we also add lesion labels (obtained by running FreeSurfer on the corresponding T1 scan) with 50% probability to build robustness to white matter lesions (Supplement 3). Finally, the training label maps are randomly right/left flipped, and randomly cropped to  $160^3$  volumes for memory constraints.

### 3.3 Competing methods

We compare SynthSeg against five other approaches:

**T1 baseline:** This baseline refers to a supervised network trained with real T1 scans from the same subjects as for SynthSeg (Table 1). This approach aims at: (i) comparing the effect of training a network with real instead of synthetic images, and (ii) assessing the generalisation of supervised networks on scans of the same MR modality (T1) but of variable contrasts. We retrain a specific network to segment data at all the 10 tested resolutions (i.e., 1 mm<sup>3</sup>, and 3, 5, and 7 mm in axial/coronal/sagittal directions, see Section 3.1).

For comparison purposes, we reemploy the same UNet architecture and augmentation scheme (i.e., spatial deformation, intensity augmentation, bias field corruption) as for SynthSeg. Furthermore, we also apply white noise injection, with a standard deviation sampled at each mini-batch in  $\mathcal{U}[0, 20]$  (assuming an input in the  $[0, 255]$  interval). We emphasise that this network can only segment T1 scans (Dice scores are below 0.01 when applied to other modalities).

**Test time adaptation (TTA):** We also compare SynthSeg against a state-of-the-art domain adaptation approach using a TTA strategy [77] (similar to [78]). We believe that TTA is a natural competitor for SynthSeg, since it can adapt to unseen domains with light fine-tuning, as opposed to unsupervised domain adaptation, which needs to be retrained from scratch for every new target domain.

This method is based on three CNN modules: an image normaliser (5 convolutional layers), a segmentation UNet, and a denoising auto-encoder (DAE, with 4 levels). At first, the normaliser and the Unet are jointly trained on supervised data, and the DAE is trained only on segmentations. At test time, the Unet and DAE are frozen, while the normaliser is fine-tuned on each scan by optimising the average Dice between the Unet predictions and their counterparts denoised by the DAE. However, since the first predictions can be quite erroneous (which the DAE cannot correct), the loss is initially optimised with respect to an atlas. Then, as soon as a double threshold criterion is met [77], the training continues with the DAE-based loss until convergence, which takes around an hour for the first scan of a new domain, and several minutes for subsequent images of the same domain. We employ the same UNet architecture and augmentation scheme as for SynthSeg. The list of changes relatively to the original paper is detailed in Supplement 4.

**SAMSEG:** We also assess the performance of SAMSEG [108], which is based on the traditional Bayesian segmentation framework with unsupervised likelihood distributions. As such, SAMSEG is fully contrast-adaptive, and can segment scans at any resolution, even though it does not account for Partial Volume effects (see Section 1.3). In contrast with CNN-based approaches, SAMSEG does not need to be trained as it uses its own optimisation framework, which runs in approximately 12 minutes per scan.

**SynthSeg variants:** Finally we compare SynthSeg against two variants to validate different aspects of the proposed method. In the first variant, called SynthSeg-R, we train resolution-specific networks for each of the 10 testing resolutions. We then further constrain the synthesis by training another set of networks, named SynthSeg-RC, that are specific to both contrast and resolution. In this variant, we employ normal priors over the GMM parameters, which are estimated on each target domain as follows: (i) we segment a few scans with SAMSEG, (ii) use the obtained segmentations to estimate the normal priors over  $M_G$  and  $\Sigma_G$  (see Section 2.1.2), and (iii) artificially increase the variances by a factor of 3 for improved generalisation [81], [87]. Overall, SynthSeg-R aims at assessing the effect of randomising the resolution during training, while SynthSeg-RC enables to study the impact of generating random against realistic contrasts at a given resolution.

The predictions of all methods are postprocessed as de-



scribed in Section 2.3, except for SAMSEG that we use out-of-the-box, but for which we still upsample test scans to 1 mm resolution. Similarly to SynthSeg, all learning-based methods are retrained twice, and results are reported for the model obtaining the best scores on the validation set.

### 3.4 Evaluation metrics

We measure the similarity between the output segmentations and their ground truth by first computing the average (hard) Dice score over all predicted labels. If  $Y = \{Y_i\}$  is the binary mask of a predicted structure and  $T = \{T_i\}$  is its corresponding ground truth, their Dice score is given by:

$$Dice(Y, T) = 2 \times \frac{\sum_i Y_i T_i}{\sum_i Y_i + \sum_i T_i}. \quad (7)$$

We also compute surface-to-surface distances in millimetres for each label, and report the average 95<sup>th</sup> percentile value (SD95) as a robust version of the Hausdorff distance. Note that one typically wishes to obtain high Dice scores (with 1 being the best score) and to achieve low SD95 values (with 0 indicating a perfect segmentation). These evaluation metrics are complementary, since Dice coefficients measure the general structure alignment, while SD95 is sensitive to morphological outliers.

## 4 EXPERIMENTS AND RESULTS

In this section, we present four sets of experiment to validate the accuracy and generalisation ability of the proposed framework. First, we compare SynthSeg against all competing methods, and evaluate its adaptability to different modalities and resolutions. The second experiment assesses the performance of SynthSeg in a multi-modality setting. In the third experiment, we study the impact of the number and origin (i.e., manual or automated) of the training segmentations. Finally, we validate SynthSeg in a volumetric group study, which represents one of the main applications that we envision for our publicly available tool.

### 4.1 Robustness to contrast and resolution

In this experiment, we test SynthSeg on a variety of contrasts and resolutions to assess its generalisation ability. This is achieved by comparing the proposed approach against all competing methods for every dataset at native resolution. The results are summarised in Table 2 and Figure 4.

On the one hand, having access to real intensity distributions during training, the T1 baseline and the TTA framework excel when tested on held-out scans of their source domain (namely T1-39, HCP, and ADNI). They yield the best Dice coefficients for all three datasets (with an outstanding Dice scores of 0.91 on T1-39), and the lowest SD95 for T1-39 and ADNI. When testing SynthSeg on these datasets, we observe that it also obtains very good results, even though it has never seen a real image during training. Specifically, SynthSeg reaches nearly the level of accuracy of the T1 baseline and the TTA framework, as it exhibits slightly lower Dice (especially for HCP and ADNI, for which the difference is only 0.01), and even yields the best average SD95 for the HCP dataset.

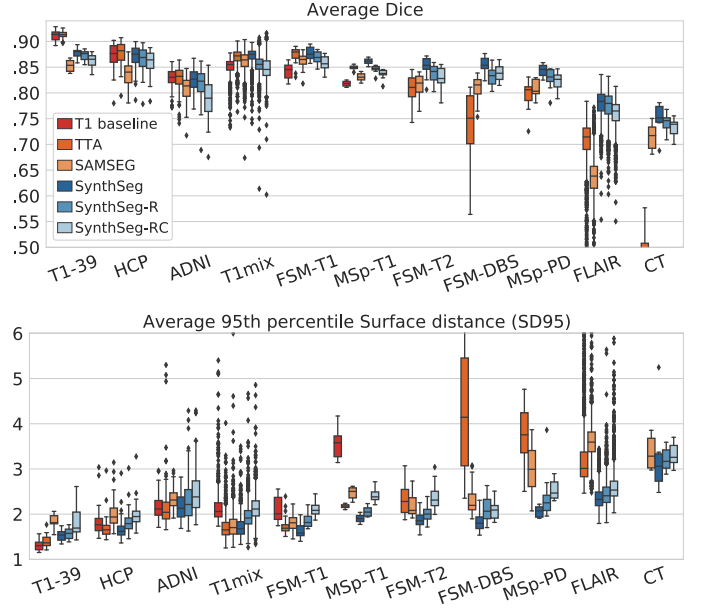


Fig. 4. Box plots showing Dice scores and SD95 (in mm) obtained by all methods for every dataset at 1mm isotropic resolution (except for FLAIR and CT, which are at 3mm and 5mm axial resolution, respectively), and averaged across all evaluated structures. For each box, the central mark is the median; edges are the first and third quartiles; whiskers extend to 1.5 interquartile ranges; and outliers are marked with  $\blacklozenge$ .

On the other hand, the domain randomisation strategy makes SynthSeg robust against changes in contrast and resolution. This is exemplified in Figure 5, which shows high-level feature maps for a 1 mm T1 and a 5 mm axial T2 of the same subject. While the features produced by the T1 baseline quickly degrade on the T2 scan, SynthSeg produces features that are almost identical for both modalities. This is despite the lower resolution of the T2 scan, whose features are effectively super-resolved to 1 mm resolution.

The robustness of SynthSeg translates into outstanding generalisation, as it yields the best scores in almost all target domains (T1mix, FSM, MSp, FLAIR, and CT), 5 of which are statistically significant for Dice and 7 for SD95 (Table 2). Overall, SynthSeg maintains a relatively constant accuracy throughout all tested contrasts and resolutions (Figures 4 and 6). This is in contrast with the T1 baseline, whose performance slightly decays when presented with T1 scans of different contrasts (e.g. SD95 = 3.57 mm for MSp-T1). Fine-tuning the TTA framework on each target domain enables it to alleviate this problem for intra-modality applications (e.g., 0.03 Dice improvement relatively to the T1 baseline for FSM-T1). Nevertheless, substantial fluctuations in the TTA results are still observed for larger domain gaps (e.g., SD95 = 4.54 mm for FSM-DBS, and Dice = 0.44 for CT).

In comparison, SAMSEG yields uniform results for T1 scans, where it significantly outperforms the T1 baseline outside its training domain (Table 2). It also produces high quality segmentations for non-T1 modalities at 1 mm resolution (i.e., FSM-T2, FSM-DBS, MSp-PD), yielding better scores than TTA, especially for FSM-DBS scans (0.11 Dice and 2.2 mm SD95 improvements). However, we can see a considerable drop in accuracy when SAMSEG is tested on LR scans with PV effects: it decreases to 0.71 Dice on the CT

TABLE 2

Mean Dice score and 95<sup>th</sup> percentile surface distance (SD95), obtained by all methods for every dataset at 1mm isotropic resolution (except for FLAIR and CT, at 3mm and 5mm axial resolution respectively), and averaged across all evaluated structures. The best scores for each dataset are in bold, and marked with a star if significantly better than all other methods at a 1% level (two-sided non-parametric Wilcoxon signed-rank test).

		T1-39	HCP	ADNI	T1mix	FSM-T1	MSP-T1	FSM-T2	FSM-DBS	MSP-PD	FLAIR	CT
T1 baseline	Dice	0.91	0.87	0.83	0.85	0.84	0.82	N/A	N/A	N/A	N/A	N/A
	SD95	<b>1.31*</b>	1.8	<b>2.15*</b>	2.24	2.12	3.57	N/A	N/A	N/A	N/A	N/A
TTA	Dice	0.91	<b>0.88*</b>	0.83	0.87	0.87	0.85	0.81	0.7	0.8	0.7	0.44
	SD95	1.4	1.68	2.2	1.75	1.77	2.17	2.35	4.54	3.75	4.04	21.0
SAMSEG	Dice	0.85	0.84	0.81	0.86	0.86	0.83	0.82	0.81	0.81	0.64	0.71
	SD95	1.85	2.0	2.34	1.77	1.81	2.47	2.21	2.34	2.99	3.67	3.36
SynthSeg	Dice	0.88	0.87	0.82	0.87	<b>0.88</b>	<b>0.86*</b>	<b>0.85*</b>	<b>0.86*</b>	<b>0.84*</b>	<b>0.78*</b>	<b>0.75</b>
	SD95	1.53	<b>1.66</b>	2.16	<b>1.73*</b>	<b>1.62*</b>	<b>1.9*</b>	<b>1.87*</b>	<b>1.82*</b>	<b>2.06*</b>	<b>2.38*</b>	3.31
SynthSeg-R	Dice	0.87	0.87	0.82	0.85	0.87	0.85	0.84	0.83	0.83	0.77	0.74
	SD95	1.58	1.81	2.31	2.1	1.86	2.06	2.01	2.13	2.44	2.51	<b>3.21</b>
SynthSeg-RC	Dice	0.86	0.86	0.79	0.85	0.86	0.84	0.83	0.84	0.82	0.76	0.73
	SD95	1.84	1.97	2.5	2.3	2.11	2.42	2.37	2.09	2.54	2.86	3.32

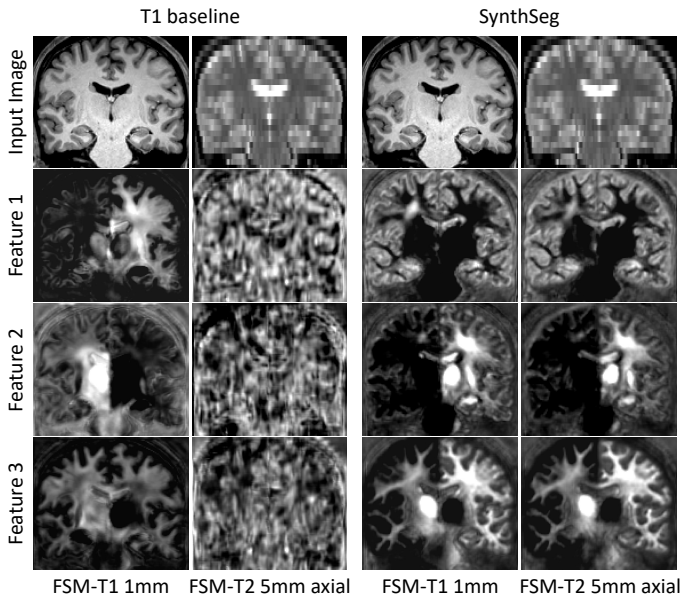


Fig. 5. Representative features of the last layer of the network in response to two scans of different contrast and resolution for the same subject. While SynthSeg builds a consistent representation across contrasts and resolutions, the T1 baseline only produces noise for scans outside its training domain.

dataset (3 mm axial), and to 0.64 on the FLAIR data (5 mm axial) where it lies 14 points behind SynthSeg.

Crucially, narrowing the distributions of the generation parameters (to simulate scans of a specific contrast and/or resolution) consistently decreases the accuracy of the results, despite retraining for each target domain (Figure 4). Specifically, the Dice scores for SynthSeg-R are on average lower than SynthSeg by 1.1 point, and SD95 is 0.18 mm worse. This difference grows when the intensity distributions are further constrained to represent realistic contrasts, resulting in gaps of 2 Dice points and 0.39 mm in SD95 for SynthSeg-RC.

To further validate the adaptiveness of the proposed approach to differences in resolution, we test SynthSeg on

all artificially downsampled datasets (Table 1). In addition to SynthSeg, this study compares T1 baselines retrained to segment at each target resolutions, as well as SAMSEG, which does not need to be retrained. We do not include TTA, SynthSeg-R, or SynthSeg-RC, since all have been shown to be significantly outperformed by SynthSeg.

The results, illustrated in Figure 7 and Figure 8, show that SynthSeg maintains a very good accuracy for all tested resolutions. Despite the considerable loss of information at LR, SynthSeg only loses an average 3.9 Dice points between 1 mm and 7 mm slice spacing. However, we note a slight decrease in accuracy for thin and convoluted structures such as the cortex. Meanwhile, SAMSEG exhibits a much higher drop in performance as it decreases on average by 7.6 Dice points across the range of tested resolutions. As before, the T1 baselines obtain outstanding results on scans similar to their training data, but poorly generalise to unseen domains (i.e., FSM-T1 and MSP-T1), where SynthSeg is clearly superior. Moreover, we note that the difference between the two on T1-39 progressively reduces for lower resolutions until it reaches a very thin margin for 7 mm data, which shows that the difference between using real or random synthetic intensity profiles greatly narrows at LR.

## 4.2 SynthSeg in multi-modality settings

The second experiment evaluates SynthSeg in a multi-modality setting. This is a frequent scenario in the clinic, where physicians typically acquire several contrasts in different directions to obtain complementary imaging data for diagnosis. Therefore, we simulate three multi-modality datasets representative of clinical acquisitions: (i) T1 and T2 FSM scans at 5 mm coronal and 3 mm sagittal, (ii) T1 and DBS FSM data at 5 mm sagittal and 5 mm axial, and (iii) T1 and PD MSP scans at 5 mm sagittal and 7 mm sagittal.

To assess the advantage of using multi-modality data, we retrain SynthSeg once to take two channels (of any contrast and resolution) as input. We then compare this new version against its single-modality equivalent, run independently

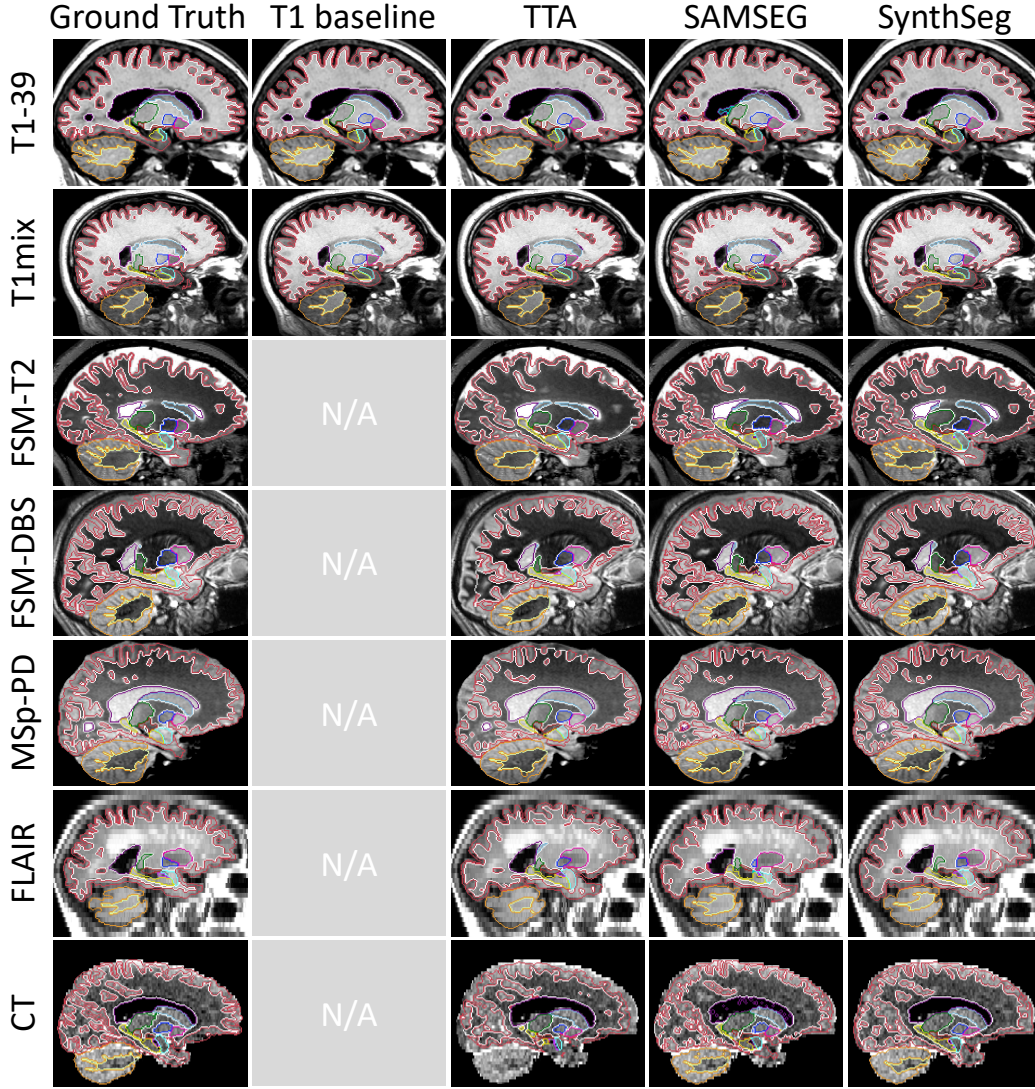


Fig. 6. Sample segmentations from the first experiment. SynthSeg remarkably generalises to all contrasts and resolutions, and produces very accurate segmentations. In comparison the T1 baseline obtains remarkable results on data similar to its training domain, but cannot be applied to other contrasts. While the TTA approach yields outstanding segmentations for T1 T1-39 and T1mix, its results degrade for larger domain gaps. This is particularly noticeable for the cortex (red label), which presents major mistakes in all non-T1 modalities. Finally, SAMSEG yields coherent results for all scans at 1 mm resolution, but is heavily affected by PV effects at LR (see lateral ventricle, in dark purple, for FLAIR and CT scans).

on each channel. We also report results achieved by averaging the posteriors obtained by the uni-modality SynthSeg for each channel, which aims at assessing the impact of processing the images jointly or separately.

Table 3 shows that retraining SynthSeg on several channels yields better results than segmenting only one of them. However, this improvement is limited, especially with respect to the T1 inputs, which in general yield better structure contrasts, (maximum difference of 0.02 Dice), except for T1-DBS where the SD95 increases by 0.16 mm. In comparison, naïvely averaging the posteriors of the uni-modality SynthSeg has two opposite effects. While this method enables to almost bridge the Dice gap (no difference with multi-modality SynthSeg for T1-T2, and T1-DBS), it also deteriorates the surface distances (now higher than for the T1 channels for T1-T2 and T1-PD). Overall, these results show that a multi-modality network leads to a slight increase in accuracy with respect to the highest-quality input.

### 4.3 Impact of the source and number of training label maps

In this experiment, we evaluate the accuracy of SynthSeg as a function of the number of segmentations used during training, as well as their source (manual or automated). We first train SynthSeg on increasing numbers of label maps ( $N \in \{1, 5, 10, 15, 20\}$ ), randomly taken from the T1-39 dataset. For each value of  $N$ , we retrain SynthSeg  $n_N$  times, where  $n_N$  is higher for lower values of  $N$  to compensate for the greater variability in the random subject selection (Supplement 5). In addition, we include the version of SynthSeg trained on all available maps (manual and automated). This enables us to quantify the effect of adding a considerable amount of automated segmentations from diverse populations (young and healthy, ageing and AD) to the training set. Once all networks are trained, we assess them on six representative datasets: T1mix (1 mm isotropic), FSM-T2 (3 mm coronal resolution), MSP-T1 (7 mm sagittal), MSP-



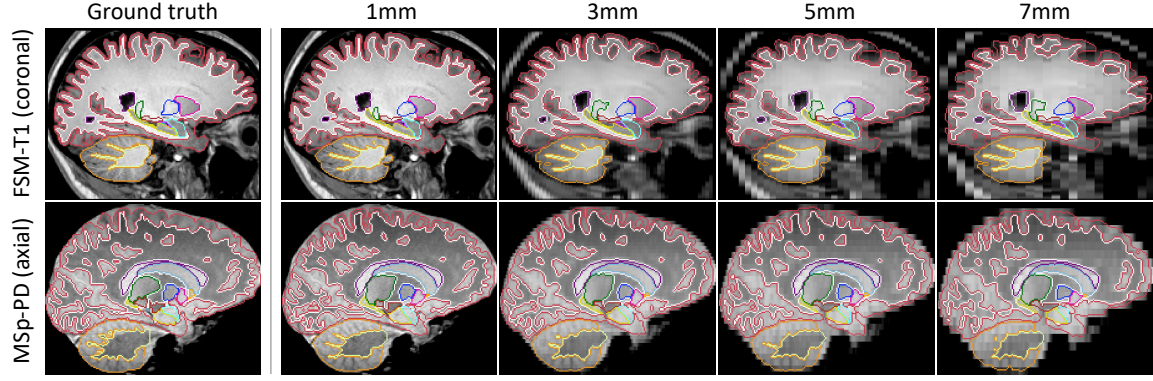


Fig. 7. Examples of segmentations obtained by SynthSeg for two scans artificially downsampled at decreasing LR. SynthSeg presents an impressive generalisation ability to all resolutions, despite heavy PV effects and important loss of information at LR. However, we observe a slight decrease in accuracy for thin and convoluted structures such as the cerebral cortex (red) or the white cerebellar matter (dark yellow).

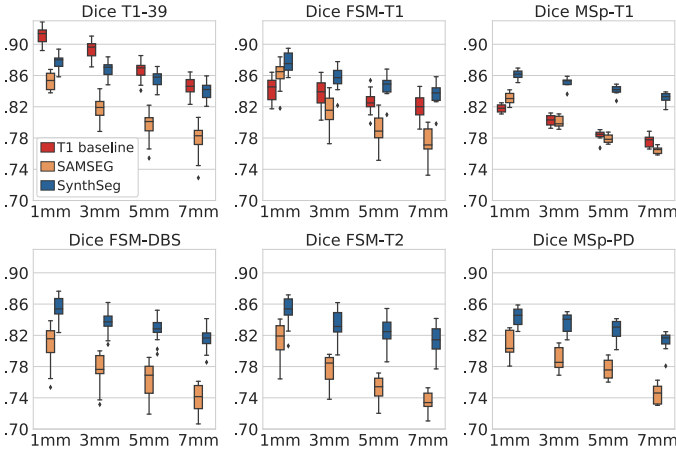


Fig. 8. Box plots showing Dice scores for data artificially downsampled at different resolutions. Results are obtained by evaluating Dice coefficients at 3, 5, and 7 mm resolutions in axial, coronal, and sagittal directions, and averaging them across acquisition directions.

TABLE 3  
Scores obtained in three multi-modality settings: FSM T1 (5mm coronal)-T2 (3mm sagittal), FSM T1 (5mm sagittal)-DBS (5mm axial), and MSP T1 (5mm coronal)-PD (7mm sagittal).

		T1-T2	T1-DBS	T1-PD
SynthSeg 1 <sup>st</sup> channel	Dice	0.85	0.84	0.85
	SD95	1.81	1.89	2.01
SynthSeg 2 <sup>nd</sup> channel	Dice	0.83	0.84	0.80
	SD95	2.0	1.97	2.59
SynthSeg av. posteriors	Dice	0.85	0.86	0.84
	SD95	1.84	1.76	2.11
SynthSeg multi-modal	Dice	0.85	0.86	<b>0.86</b>
	SD95	<b>1.77*</b>	<b>1.73*</b>	<b>2.0</b>

PD (5 mm coronal), FLAIR (5 mm axial) and ADNI (1 mm isotropic). T1 mix aims at assessing robustness against variations in T1 contrast; FSM-T2 and MSP (T1 and PD) enable to further diversify the test data in terms of contrasts and resolutions; and FLAIR and ADNI scans permit us to assess generalisation to different populations (ageing and AD).

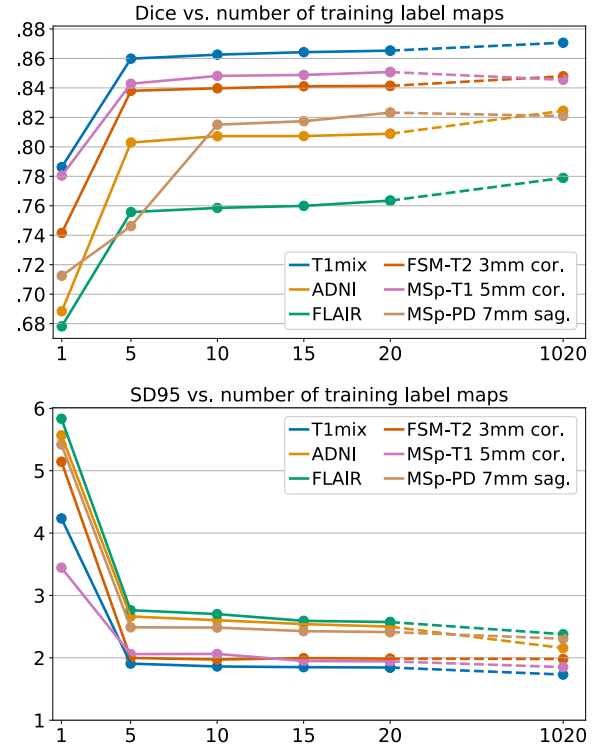


Fig. 9. Dice and SD95 (in mm) vs. number of training label maps, for representative datasets. The last points are obtained when training on all available labels maps (20 manual plus 1,000 automated).

The average Dice and SD95 obtained for every  $N$  are plotted in Figure 9. They reveal that using only one training subject already attains decent Dice scores (between 0.67 and 0.79 for all datasets), but still yields high surface distances (between 3 and 6 mm) due to the limited robustness against changes in morphology. As expected, the accuracy of the produced segmentations increases when adding more training labels. However, this improvement quickly becomes marginal, and the accuracy plateaus at  $N = 5$  subjects (except for MSP-PD, for which levels off at 10 label maps). Indeed, Dice scores and SD95 only change by a maximum of 0.5 points and 0.15 mm between  $N = 5$  and  $N = 20$ .

Meanwhile, adding a large amount of automated label maps to the training set produces a slight increase in *av-*



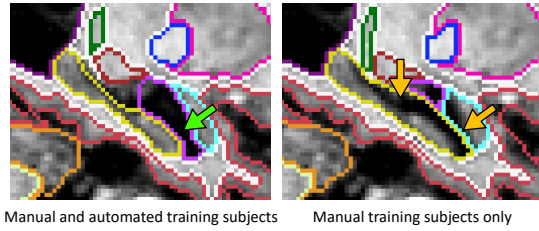


Fig. 10. Close-up on the hippocampal area for a representative ADNI subject with severe AD atrophy. Adding automated label maps from different populations to the training set improves robustness against morphological variability (green arrow) over training only with manual segmentations (orange arrows).

erage performance. Moreover, the improvement is slightly higher for the ADNI and FLAIR datasets, where Dice scores increase by 1.8 and 1.9 Dice points, and SD95 decreases by 0.35 mm and 0.26 mm respectively. This result is even more pronounced when investigating results for the 1% of ADNI subjects with the largest ventricular volumes (corrected for Intra-Cranial Volume, ICV), which we use as a proxy for severity of AD. They reveal that for subjects with severe atrophy, Dice scores increase by 5 points and SD95 decrease by 0.5 mm relatively to the network trained only on T1-39 manual segmentations. This is exemplified in Figure 10, which shows that the network trained on the manual delineations has trouble generalising to subjects with severe AD atrophy, whereas the version with the augmented training set reliably segments such subjects.

#### 4.4 Alzheimer’s Disease volumetric study

In the fourth experiment, we evaluate SynthSeg in a neuroimaging group study, which represents a main application that we envision for our method. The scans used in this experiment are a separate set of 100 unpreprocessed T1 and FLAIR scans from ADNI, at 1 mm isotropic and 5 mm axial resolution. Specifically, we conduct a volumetric study to indirectly evaluate the accuracy of SynthSeg by assessing its ability to detect atrophy patterns in AD patients [109]. This is achieved by measuring effect sizes in the hippocampal volume between controls and diseased subjects, a thoroughly analysed biomarker for AD [110], with Cohen’s  $d$  [111]. If  $\mu_C$ ,  $s_C^2$  and  $\mu_{AD}$ ,  $s_{AD}^2$  are the means and variances of two samples of size  $n_C$  and  $n_{AD}$ , where  $C$  stands for Controls and  $AD$  for AD subjects, Cohen’s  $d$  is given by:

$$d = \frac{\mu_C - \mu_{AD}}{s}, \quad s = \sqrt{\frac{(n_C - 1)s_C^2 + (n_{AD} - 1)s_{AD}^2}{n_C + n_{AD} - 2}}. \quad (8)$$

An effect size is considered small if its Cohen’s  $d$  is lower than 0.2, and large if it is above 0.8 [111].

In this experiment, we compare the Cohen’s  $d$  yielded by SynthSeg and SAMSEG against a silver standard obtained by running FreeSurfer on the T1 scans [69]. We compute the hippocampal volumes by summing the values of the corresponding posteriors (i.e. soft volumes), which enables us to account for segmentation uncertainties. All measured volumes are corrected for age, gender, and ICV using a general linear model. The ICVs are estimated with FreeSurfer [69].

TABLE 4  
Effect size (Cohen’s  $d$ ) obtained by FreeSurfer (Ground Truth), SAMSEG and SynthSeg for hippocampal volumes between controls and AD patients for different types of scans.

Contrast	Resolution	FreeSurfer (GT)	SAMSEG	SynthSeg
T1	1 mm <sup>3</sup>	1.38	1.46	1.40
FLAIR	5 mm axial		0.53	1.23

The results reported in Table 4, reveal that both competing methods yield a Cohen’s  $d$  close to the ground truth for 1 mm isotropic T1 scans. However, the accuracy of SAMSEG considerably degrades on FLAIR scans, for which it obtains less than half of the expected effect size ( $d = 0.53$  vs.  $d = 1.38$ ). In contrast, SynthSeg sustains a high level of accuracy on the FLAIR scans, producing a Cohen’s  $d$  equal to 1.23, almost as high as the reference ground truth value, which was obtained on the T1 scans of much better quality.

## 5 DISCUSSION

In this article, we have presented SynthSeg, a learning strategy for robust segmentation of brain scans of any contrast and resolution. The main contribution is a new domain randomisation strategy, where a segmentation network is trained with synthetic scans of fully randomised contrast, resolution, and shape, controlled by parameters sampled from uninformative uniform priors. By producing highly diverse samples, this approach forces the network to learn domain-agnostic features. As a result, SynthSeg only needs to be trained once, and can readily segment any brain MRI scan. The outstanding flexibility of SynthSeg is demonstrated in the first experiment, where it maintains a remarkable accuracy across a wide array of scans spanning different contrasts and resolutions, with or without preprocessing, and from different subject populations (from young and healthy to ageing and diseased).

Overall, SynthSeg yields almost the same accuracy as supervised networks on their training domain, and sustains this level of performance on all test datasets. This is in contrast with the T1 baseline, whose results deteriorate slightly on unseen T1 datasets, although it was trained on a large number of scans and with the same aggressive data augmentation as SynthSeg. This finding underscores the difficulty of segmenting unpreprocessed scans of different domains, even within the same MR modality. Moreover, when comparing SynthSeg with supervised networks re-trained at different resolutions, we see that the gap in accuracy on the training domain nearly vanishes at very low resolution. This is likely due to the fact that the domain gap between real and synthetic contrasts mainly lies in higher frequencies, and progressively fades at lower resolutions. As a result, this makes SynthSeg particularly useful when tested on scans with lower resolutions.

Employing supervised CNNs in a TTA approach considerably increases their generalisation ability. By fine tuning a few convolutional layers on each target domain, this strategy increases the scores obtained by supervised networks on unseen data, even if preprocessed differently (e.g., with

skull stripping). Moreover, TTA can segment modalities distinct from its training domain, which is unfeasible with fully supervised networks alone. While TTA obtains outstanding results for smaller domain gaps, its performance can greatly degrade on scans of different MR modality and resolution (e.g., the FLAIR and CT datasets). This is despite our efforts to adapt the competing TTA method [77] to our application, which increased Dice by approximately 20 points compared with the original implementation. More generally, TTA is outperformed by SynthSeg for all target domains, while still requiring to be fine-tuned (thus needing more time and computational resources), and necessitating the injection of *a priori* anatomical knowledge with a registered atlas. This outcome highlights the benefit of using a domain randomisation approach over state-of-the-art domain adaptation strategies.

As opposed to TTA, which requires fine-tuning on each test scan, SAMSEG readily achieves contrast-independence. However, it still needs to perform Bayesian inference via iterative optimisation on each test scan, and thus runs considerably slower than SynthSeg. While SAMSEG is consistently outperformed by SynthSeg for all datasets, it generally yields more robust segmentations than supervised CNNs and TTA on unseen data at 1 mm<sup>3</sup> resolution. However, its accuracy declines considerably when applied to LR scans, since it does not model PV effects. This is in contrast to SynthSeg, which remains robust to changes in resolution, even for high slice spacing and thickness.

Importantly, the impact of randomising the model parameters is demonstrated by the higher performance of SynthSeg relatively to its domain-constrained variants. Training a resolution-specific version of SynthSeg leads to a consistent decrease in accuracy, regardless of the testing resolution and contrast. Additionally, narrowing the parameters of the GMM to yield contrast-specific samples further deteriorates the results. We believe this outcome is likely a combination of two phenomena. First, randomising the generation parameters enables us to mitigate the inaccuracies in the assumptions made when designing the model (e.g., Gaussian intensity distributions, simulation of slice selection profiles, etc.). Second, this result is consistent with converging evidence that augmenting the data beyond realism often leads to more robust models that generalise better [28], [29], [30], [31].

We have tested SynthSeg in three different multi-modality settings, where training to simultaneously segment two inputs exhibits slightly better results than separately processing them with a uni-modality version of SynthSeg. Specifically, we observe that the increase in accuracy is less pronounced for the channel of higher tissue contrast (generally a T1). This suggests that the multi-modality network is mainly driven by the channel of higher quality, while still exploiting information from the second channel, hence leading to a consistent improvement over either input. While averaging posteriors separately obtained by the uni-modality CNN enables us to improve Dice scores with respect to not sharing knowledge between channels, this method degrades surface distances. This can be explained by the fact that posteriors obtained separately from different channels do not generally overlap perfectly, and averaging them creates edge artefacts that have little impact

on Dice but lead to higher SD95. We stress that the results reported in this experiment are obtained using high quality multi-modality scans that, unlike clinical images, are almost perfectly aligned. A more thorough evaluation on multi-modality clinical dataset will be needed to assess the impact of imperfect channel registration on SynthSeg.

The third experiment shows that, thanks to its aggressive spatial augmentation and domain randomisation, SynthSeg does not need much data to produce satisfactory results: after five training label maps, the average improvement in Dice and SD95 is very small. On the other hand, further inclusion of automated label maps in the training set greatly improves robustness, especially if such maps are from different populations. Specifically, augmenting the morphological variability in the training dataset enables SynthSeg to produce robust segmentations, even for AD patients with severe atrophy.

Finally, the fourth experiment shows that SynthSeg is able to detect atrophy patterns related to AD [109]. We emphasise that, while this task is of modest complexity for 1 mm T1 scans (where all methods produce satisfactory results), segmenting the hippocampus in 5 mm FLAIR scans is much more difficult, especially due to their axial orientation: since the main axis of the hippocampus is approximately parallel to the acquisition plane, this structure only appears in very few slices (2.7 on average), and with heavy PV. As a result, the accuracy of SAMSEG considerably degrades on the FLAIR scans. In contrast, SynthSeg achieves almost the same accuracy as one of the most widespread neuroimaging packages [69], while only having access to the lower quality FLAIR scans. This suggests that SynthSeg can reliably be used in neuroimaging studies of clinical scans, which represent a main application envisioned for the released model.

## 6 CONCLUSION

Overall, SynthSeg can segment brain MRI scans of any contrast and resolution without requiring retraining or fine-tuning. The proposed method is demonstrated across 5,500 scans spanning 8 datasets, 6 MRI modalities and 10 resolutions, where it maintains a uniform accuracy and almost attains the performance of supervised CNNs on their training domain. SynthSeg also obtains scores similar to state-of-the-art domain adaptation methods for small domain gaps, while considerably outperforming them for larger domain gaps. Furthermore, the presented method is consistently more accurate than Bayesian segmentation, while being able to cope with PV effects in LR scans and running in a fraction of the time. Finally, SynthSeg can reliably be used in neuroimaging studies with clinical scans, as it detects atrophy patterns linked with AD for LR clinical images.

While the main focus of this article was on the use of domain randomisation to segment scans of arbitrary contrasts and resolutions, future work will aim at extending SynthSeg to reach the level of supervised networks on their training domain. We will explore the use of other CNN architectures to replace the UNet employed in this work: while Unets are widely used for medical images, other networks may yield increased performance. Another possible improvement could be to append an adversarial network to the generative model in order to bridge the domain gap

between real and synthetic contrasts. Finally, we plan to investigate the use of auto-encoders trained on label maps to “denoise” the output segmentations and further increase the robustness of SynthSeg.

The code and trained model are publicly available at <https://github.com/BBillot/SynthSeg>. In contrast with other deep learning methods, SynthSeg does not need to be retrained or fine-tuned on unseen datasets, so it can be used out of the box and yield easily reproducible results. Moreover, relying on a single, publicly available, model will greatly facilitate the use of SynthSeg by neuroimaging researchers, since it eliminates the need for retraining, and thus the associated requirements in terms of hardware and deep learning expertise.

By producing robust segmentations of nearly any brain MRI scan with an open-source implementation, SynthSeg will enable quantitative analyses of huge amounts of existing clinical MRI data, which could greatly improve the characterisation and diagnosis of neurological disorders.

## ACKNOWLEDGEMENTS

This research was supported by the European Research Council (ERC Starting Grant 677697, project BUNGEE-TOOLS), the EPSRC-funded UCL Centre for Doctoral Training in Medical Imaging (EP/L016478/1) and the Department of Health’s NIHR-funded Biomedical Research Centre at University College London Hospitals. Further support was provided by Alzheimer’s Research UK (ARUK-IRG2019A-003), the NIH BRAIN Initiative (RF1-MH123195 and U01-MH117023), the National Institute for Biomedical Imaging and Bioengineering (P41-EB015896, 1R01-EB023281, R01-EB006758, R21-EB018907, R01-EB019956), the National Institute on Aging (1R01-AG070988, 1R56-AG064027, 5R01-AG008122, R01-AG016495, 1R01-AG064027), the National Institute of Mental Health the National Institute of Diabetes and Digestive and Kidney Diseases (1-R21-DK-108277-01), the National Institute for Neurological Disorders and Stroke (R01-NS112161, R01-NS0525851, R21-NS072652, R01-NS070963, R01-NS083534, 5U01-NS086625, 5U24-NS10059103, R01-NS105820), the Shared Instrumentation Grants 1S10-RR023401, 1S10-RR01-9307, and 1S10-RR023043, the Lundbeck foundation (R313-2019-622), and the NIH Blueprint for Neuroscience Research (5U01-MH093765), part of the Human Connectome Project.

The collection and sharing of the ADNI data used here was funded by the Alzheimer’s Disease Neuroimaging Initiative (National Institutes of Health Grant U01 AG024904) and Department of Defence (W81XWH-12-2-0012). ADNI is funded by the National Institute on Aging, the National Institute of Biomedical Imaging and Bioengineering, and by the following: Alzheimer’s Association; Alzheimer’s Drug Discovery Foundation; BioClinica, Inc.; Biogen Idec Inc.; Bristol-Myers Squibb Company; Eisai Inc.; Elan Pharmaceuticals, Inc.; Eli Lilly and Company; F. Hoffmann-La Roche Ltd and affiliated company Genentech, Inc.; GE Healthcare; Innogenetics, N.V.; IXICO Ltd.; Janssen Alzheimer Immunotherapy Research & Development, LLC.; Johnson & Johnson Pharmaceutical Research & Development LLC.; Medpace, Inc.; Merck & Co., Inc.; Meso Scale Diagnostics,

LLC.; NeuroRx Research; Novartis Pharmaceuticals Corporation; Pfizer Inc.; Piramal Imaging; Servier; Synarc Inc.; and Takeda Pharmaceutical Company. The Canadian Institutes of Health Research is providing funds to support ADNI clinical sites in Canada. Private sector contributions are facilitated by the Foundation for the National Institutes of Health. The grantee organisation is the Northern California Institute for Research and Education, and the study is coordinated by the Alzheimer’s Disease Cooperative Study at the University of California, San Diego. ADNI data are disseminated by the Laboratory for Neuro Imaging at the University of Southern California.

## REFERENCES

- [1] D. Tisserand, J. Pruessner, E. Sanz Arigita, M. van Boxtel, A. Evans, J. Jolles, and H. Uylings, “Regional frontal cortical volumes decrease differentially in aging: an MRI study to compare volumetric approaches and voxel-based morphometry,” *NeuroImage*, vol. 17, pp. 57–69, 2002.
- [2] S. Warfield, K. Zou, and W. Wells, “Simultaneous truth and performance level estimation: an algorithm for the validation of image segmentation,” *IEEE Transactions on Medical Imaging*, vol. 23, no. 7, pp. 903–921, 2004.
- [3] O. Ronneberger, P. Fischer, and T. Brox, “U-Net: Convolutional Networks for Biomedical Image Segmentation,” in *Medical Image Computing and Computer-Assisted Intervention*, 2015, pp. 234–241.
- [4] F. Milletari, N. Navab, and S. Ahmadi, “V-Net: Fully Convolutional Neural Networks for Volumetric Medical Image Segmentation,” in *International Conference on 3D Vision*, 2016, pp. 565–571.
- [5] K. Kamnitsas, C. Ledig, V. Newcombe, J. Simpson, A. Kane, D. Menon, D. Rueckert, and B. Glocker, “Efficient multi-scale 3D CNN with fully connected CRF for accurate brain lesion segmentation,” *Medical Image Analysis*, vol. 36, pp. 61–78, 2017.
- [6] R. Müller, P. Shih, B. Keehn, J. Deyoe, K. Leyden, and D. Shukla, “Underconnected, but How? A Survey of Functional Connectivity MRI Studies in Autism Spectrum Disorders,” *Cerebral Cortex*, vol. 21, no. 10, pp. 2233–2243, 2011.
- [7] J. Mugler and J. Brookeman, “Three-dimensional magnetization-prepared rapid gradient-echo imaging (3D MP RAGE),” *Magnetic Resonance in Medicine*, vol. 15, no. 1, pp. 152–157, 1990.
- [8] H. Choi, D. Haynor, and Y. Kim, “Partial volume tissue classification of multichannel magnetic resonance images—a mixel model,” *IEEE Transactions on Medical Imaging*, vol. 10, pp. 395–407, 1991.
- [9] K. Van Leemput, F. Maes, D. Vandermeulen, and P. Suetens, “A unifying framework for partial volume segmentation of brain MR images,” *IEEE Transactions on Medical Imaging*, vol. 22, 2003.
- [10] J. Long, E. Shelhamer, and T. Darrell, “Fully Convolutional Networks for Semantic Segmentation,” in *IEEE Conference on Computer Vision and Pattern Recognition*, 2015, pp. 3431–3440.
- [11] V. Badrinarayanan, A. Kendall, and R. Cipolla, “SegNet: A Deep Convolutional Encoder-Decoder Architecture for Image Segmentation,” *IEEE Transactions on Pattern Analysis and Machine Intelligence*, vol. 39, no. 12, pp. 2481–2495, 2017.
- [12] A. Krizhevsky, I. Sutskever, and G. Hinton, “ImageNet Classification with Deep Convolutional Neural Networks,” *Advances in Neural Information Processing Systems*, vol. 25, 2012.
- [13] K. He, X. Zhang, S. Ren, and J. Sun, “Deep Residual Learning for Image Recognition,” in *IEEE Conference on Computer Vision and Pattern Recognition*, 2016, pp. 770–778.
- [14] J. Uijlings, K. van de Sande, T. Gevers, and A. Smeulders, “Selective Search for Object Recognition,” *International Journal of Computer Vision*, vol. 104, no. 2, pp. 154–171, 2013.
- [15] S. Ren, K. He, R. Girshick, and J. Sun, “Faster R-CNN: Towards Real-Time Object Detection with Region Proposal Networks,” *IEEE Transactions on Pattern Analysis and Machine Intelligence*, vol. 39, no. 6, pp. 1137–1149, 2017.
- [16] C. Dong, C. Loy, K. He, and X. Tang, “Image Super-Resolution Using Deep Convolutional Networks,” *IEEE Transactions on Pattern Analysis and Machine Intelligence*, vol. 38, pp. 295–307, 2016.
- [17] C. Pham, A. Ducournau, R. Fablet, and F. Rousseau, “Brain MRI super-resolution using deep 3D convolutional networks,” in *IEEE International Symposium on Biomedical Imaging*, 2017, pp. 197–200.

- [18] I. J. Goodfellow, J. Pouget-Abadie, M. Mirza, B. Xu, D. Warde-Farley, S. Ozair, A. Courville, and Y. Bengio, "Generative Adversarial Networks," *arXiv:1406.2661 [cs, stat]*, 2014.
- [19] C. Ledig, L. Theis, F. Huszar, J. Caballero, A. Cunningham, A. Acosta, A. Aitken, A. Tejani, J. Totz, Z. Wang, and W. Shi, "Photo-Realistic Single Image Super-Resolution Using a Generative Adversarial Network," in *IEEE Conference on Computer Vision and Pattern Recognition*, 2017, pp. 4681–4690.
- [20] N. Jakobi, P. Husbands, and I. Harvey, "Noise and the reality gap: The use of simulation in evolutionary robotics," in *Advances in Artificial Life*, 1995, pp. 704–720.
- [21] S. Pan and Q. Yang, "A Survey on Transfer Learning," *IEEE Transactions on Knowledge and Data Engineering*, vol. 22, pp. 45–59, 2010.
- [22] A. Torralba and A. Efros, "Unbiased look at dataset bias," in *IEEE Conference on Computer Vision and Pattern Recognition*, 2011, pp. 1521–1528.
- [23] K. Kushibar, S. Valverde, S. González-Villà, J. Bernal, M. Cabezas, A. Oliver, and X. Lladó, "Supervised Domain Adaptation for Automatic Sub-cortical Brain Structure Segmentation with Minimal User Interaction," *Scientific Reports*, vol. 9, no. 1, p. 6742, 2019.
- [24] M. Orbes-Arteaga, T. Varsavsky, C. Sudre, Z. Eaton-Rosen, L. Haddow, M. Nielsen, S. Ourselin, M. Modat, P. Nachev, and M. J. Cardoso, "Multi-domain Adaptation in Brain MRI Through Paired Consistency and Adversarial Learning," in *Domain Adaptation and Representation Transfer and Medical Image Learning with Less Labels and Imperfect Data*, 2019, pp. 54–62.
- [25] L. Taylor and G. Nitschke, "Improving Deep Learning with Generic Data Augmentation," in *IEEE Symposium Series on Computational Intelligence*, 2018, pp. 1542–1547.
- [26] C. Shorten and T. Khoshgoftaar, "A survey on Image Data Augmentation for Deep Learning," *Journal of Big Data*, 2019.
- [27] E. Cubuk, B. Zoph, D. Mane, V. Vasudevan, and V. Le Quoc, "AutoAugment: Learning Augmentation Strategies From Data," in *IEEE Conference on Computer Vision and Pattern Recognition*, 2019.
- [28] K. Chaitanya, N. Karani, C. Baumgartner, A. Becker, O. Donati, and E. Konukoglu, "Semi-supervised and Task-Driven Data Augmentation," in *Information Processing in Medical Imaging*, 2019, pp. 29–41.
- [29] Y. Bengio, F. Bastien, A. Bergeron, N. Boulanger-Lewandowski, T. Breuel, Y. Chherawala, M. Cisse *et al.*, "Deep Learners Benefit More from Out-of-Distribution Examples," in *International Conference on Artificial Intelligence and Statistics*, 2011, pp. 164–172.
- [30] L. Perez and J. Wang, "The Effectiveness of Data Augmentation in Image Classification using Deep Learning," *arXiv:1712.04621 [cs]*, 2017.
- [31] A. Zhao, G. Balakrishnan, F. Durand, J. Guttag, and A. Dalca, "Data Augmentation Using Learned Transformations for One-Shot Medical Image Segmentation," in *IEEE Conference on Computer Vision and Pattern Recognition*, 2019, pp. 8543–8553.
- [32] T. Park, M. Liu, T. Wang, and J. Zhu, "Semantic Image Synthesis With Spatially-Adaptive Normalization," in *IEEE Conference on Computer Vision and Pattern Recognition*, 2019, pp. 2337–2346.
- [33] V. Sandfort, K. Yan, P. Pickhardt, and R. Summers, "Data augmentation using generative adversarial networks (CycleGAN) to improve generalizability in CT segmentation tasks," *Scientific Reports*, vol. 9, no. 1, p. 16884, 2019.
- [34] Y. Bengio, "Deep Learning of Representations for Unsupervised and Transfer Learning," in *International Conference on Machine Learning Workshop on Unsupervised and Transfer Learning*, 2012, pp. 17–36.
- [35] A. Gaidon, Q. Wang, Y. Cabon, and E. Vig, "VirtualWorlds as Proxy for Multi-object Tracking Analysis," in *IEEE Conference on Computer Vision and Pattern Recognition*, 2016, pp. 4340–4349.
- [36] Y. Zhang, S. Song, E. Yumer, M. Savva, J.-Y. Lee, H. Jin, and T. Funkhouser, "Physically-Based Rendering for Indoor Scene Understanding Using Convolutional Neural Networks," in *IEEE Conference on Computer Vision and Pattern Recognition*, 2017, pp. 5287–5295.
- [37] M. Long, Y. Cao, J. Wang, and M. Jordan, "Learning Transferable Features with Deep Adaptation Networks," in *International Conference on Machine Learning*, 2015, pp. 97–105.
- [38] Y. Ganin, E. Ustinova, H. Ajakan, P. Germain, H. Larochelle, F. Laviolette, M. Marchand, and V. Lempitsky, "Domain-Adversarial Training of Neural Networks," in *Domain Adaptation in Computer Vision Applications*, ser. Advances in Computer Vision and Pattern Recognition, 2017, pp. 189–209.
- [39] P. Isola, J. Zhu, T. Zhou, and A. Efros, "Image-To-Image Translation With Conditional Adversarial Networks," in *IEEE Conference on Computer Vision and Pattern Recognition*, 2017, pp. 1125–1134.
- [40] J. Zhu, T. Park, P. Isola, and A. Efros, "Unpaired Image-To-Image Translation Using Cycle-Consistent Adversarial Networks," in *IEEE International Conference on Computer Vision*, 2017, pp. 223–232.
- [41] J. Hoffman, E. Tzeng, T. Park, J.-Y. Zhu, P. Isola, K. Saenko, A. Efros, and T. Darrell, "CyCADA: Cycle-Consistent Adversarial Domain Adaptation," in *International Conference on Machine Learning*, 2018, pp. 1989–1998.
- [42] Q. Yang, N. Li, Z. Zhao, X. Fan, E. Chang, and Y. Xu, "MRI Cross-Modality Image-to-Image Translation," *Scientific Reports*, vol. 10, no. 1, p. 3753, 2020.
- [43] E. Todorov, T. Erez, and Y. Tassa, "MuJoCo: A physics engine for model-based control," in *IEEE/RSJ International Conference on Intelligent Robots and Systems*, 2012, pp. 5026–5033.
- [44] D. Butler, J. Wulff, G. Stanley, and M. Black, "A Naturalistic Open Source Movie for Optical Flow Evaluation," in *Computer Vision – ECCV*, 2012, pp. 611–625.
- [45] S. R. Richter, V. Vineet, S. Roth, and V. Koltun, "Playing for Data: Ground Truth from Computer Games," in *Computer Vision – ECCV*, 2016, pp. 102–118.
- [46] A. Dosovitskiy, G. Ros, F. Codevilla, A. Lopez, and V. Koltun, "CARLA: An Open Urban Driving Simulator," in *Conference on Robot Learning*, 2018.
- [47] Z. Zhang, L. Yang, and Y. Zheng, "Translating and Segmenting Multimodal Medical Volumes With Cycle- and Shape-Consistency Generative Adversarial Network," in *IEEE Conference on Computer Vision and Pattern Recognition*, 2018, pp. 242–251.
- [48] G. Louppe, J. Hermans, and K. Cranmer, "Adversarial Variational Optimization of Non-Differentiable Simulators," in *International Conference on Artificial Intelligence and Statistics*, 2019, pp. 438–447.
- [49] A. Kar, A. Prakash, M.-Y. Liu, E. Cameracci, J. Yuan, M. Rusiniak, D. Acuna, A. Torralba, and S. Fidler, "Meta-Sim: Learning to Generate Synthetic Datasets," in *IEEE International Conference on Computer Vision*, 2019, pp. 4551–4560.
- [50] J. Tremblay, A. Prakash, D. Acuna, M. Brophy, V. Jampani, C. Anil, T. To, E. Cameracci, S. Boochoon, and S. Birchfield, "Training Deep Networks With Synthetic Data: Bridging the Reality Gap by Domain Randomization," in *IEEE Conference on Computer Vision and Pattern Recognition Workshops*, 2018, pp. 969–977.
- [51] J. Tobin, R. Fong, A. Ray, J. Schneider, W. Zaremba, and P. Abbeel, "Domain randomization for transferring deep neural networks from simulation to the real world," in *IEEE/RSJ International Conference on Intelligent Robots and Systems*, 2017, pp. 23–30.
- [52] A. Sotiras, C. Davatzikos, and N. Paragios, "Deformable Medical Image Registration: A Survey," *IEEE Transactions on Medical Imaging*, vol. 32, no. 7, pp. 1153–1190, 2013.
- [53] D. Collins, C. Holmes, T. Peters, and A. Evans, "Automatic 3-D model-based neuroanatomical segmentation," *Human Brain Mapping*, vol. 3, no. 3, pp. 190–208, 1995.
- [54] T. Rohlfing, R. Brandt, R. Menzel, and C. Maurer, "Evaluation of atlas selection strategies for atlas-based image segmentation with application to confocal microscopy images of bee brains," *NeuroImage*, vol. 21, no. 4, pp. 1428–1442, 2004.
- [55] R. Heckemann, J. Hajnal, P. Aljabar, D. Rueckert, and A. Hammers, "Automatic anatomical brain MRI segmentation combining label propagation and decision fusion," *NeuroImage*, vol. 33, no. 1, pp. 115–126, 2006.
- [56] M. Sabuncu, T. Yeo, K. Van Leemput, B. Fischl, and P. Golland, "A Generative Model for Image Segmentation Based on Label Fusion," *IEEE Transactions on Medical Imaging*, pp. 714–729, 2010.
- [57] J. E. Iglesias, M. Sabuncu, and K. Van Leemput, "A unified framework for cross-modality multi-atlas segmentation of brain MRI," *Medical Image Analysis*, vol. 17, no. 8, pp. 1181–1191, 2013.
- [58] W. M. Wells, P. Viola, H. Atsumi, S. Nakajima, and R. Kikinis, "Multi-modal volume registration by maximization of mutual information," *Medical Image Analysis*, vol. 1, no. 1, pp. 35–51, 1996.
- [59] J. E. Iglesias, E. Konukoglu, D. Zikic, B. Glocker, K. Van Leemput, and B. Fischl, "Is synthesizing MRI contrast useful for inter-modality analysis?" in *Medical Image Computing and Computer-Assisted Intervention*, 2013, pp. 631–638.



- [60] G. Balakrishnan, A. Zhao, R. Sabuncu, J. Guttag, and A. Dalca, "VoxelMorph: A Learning Framework for Deformable Medical Image Registration," *IEEE Transactions on Medical Imaging*, vol. 38, no. 8, pp. 1788–1800, 2019.
- [61] K. Van Leemput, F. Maes, D. Vandermeulen, and P. Suetens, "Automated model-based tissue classification of MR images of the brain," *IEEE Transactions on Medical Imaging*, pp. 87–98, 1999.
- [62] J. Ashburner and K. Friston, "Unified segmentation," *NeuroImage*, vol. 26, no. 3, pp. 839–851, 2005.
- [63] J. E. Iglesias, J. Augustinack, K. Nguyen, C. Player, A. Player, M. Wright, N. Roy, A. McKee, L. Wald, B. Fischl, and K. Van Leemput, "A computational atlas of the hippocampal formation using ex vivo, ultra-high resolution MRI: Application to adaptive segmentation of in vivo MRI," *NeuroImage*, vol. 115, pp. 117–137, 2015.
- [64] D. Shattuck, S. Sandor-Leahy, K. Schaper, D. Rottenberg, and R. Leahy, "Magnetic Resonance Image Tissue Classification Using a Partial Volume Model," *NeuroImage*, vol. 13, pp. 856–876, 2001.
- [65] A. Jog and B. Fischl, "Pulse Sequence Resilient Fast Brain Segmentation," in *Medical Image Computing and Computer Assisted Intervention*, 2018, pp. 654–662.
- [66] B. Billot, M. Bocchetta, E. Todd, A. V. Dalca, J. D. Rohrer, and J. E. Iglesias, "Automated segmentation of the hypothalamus and associated subunits in brain MRI," *NeuroImage*, vol. 223, 2020.
- [67] N. Karani, K. Chaitanya, C. Baumgartner, and E. Konukoglu, "A Lifelong Learning Approach to Brain MR Segmentation Across Scanners and Protocols," in *Medical Image Computing and Computer Assisted Intervention*, 2018, pp. 476–484.
- [68] M. Ghafoorian, A. Mehrtash, T. Kapur, N. Karssemeijer, E. Marchiori, M. Pesteie, A. Fedorov, P. Abolmaesumi, B. Platel, and W. Wells, "Transfer Learning for Domain Adaptation in MRI: Application in Brain Lesion Segmentation," in *Medical Image Computing and Computer Assisted Intervention*, 2017, pp. 516–524.
- [69] B. Fischl, "FreeSurfer," *NeuroImage*, vol. 62, pp. 774–781, 2012.
- [70] B. Patenaude, S. Smith, D. Kennedy, and M. Jenkinson, "A Bayesian model of shape and appearance for subcortical brain segmentation," *NeuroImage*, vol. 56, no. 3, pp. 907–922, 2011.
- [71] M. Havaei, N. Guizard, N. Chapados, and Y. Bengio, "HeMIS: Hetero-Modal Image Segmentation," in *Medical Image Computing and Computer-Assisted Intervention*, 2016, pp. 469–477.
- [72] A. Chatsias, T. Joyce, M. Giuffrida, and S. Tsaftaris, "Multimodal MR Synthesis via Modality-Invariant Latent Representation," *IEEE Transactions on Medical Imaging*, vol. 37, pp. 803–814, 2018.
- [73] H.-C. Shin, H. Roth, M. Gao, L. Lu, and others, "Deep convolutional neural networks for computer-aided detection: CNN architectures, dataset characteristics and transfer learning," *IEEE Transactions on Medical Imaging*, vol. 35, no. 5, pp. 1285–1298, 2016.
- [74] D. Zhang, G. Huang, Q. Zhang, J. Han, J. Han, and Y. Yu, "Cross-modality deep feature learning for brain tumor segmentation," *Pattern Recognition*, vol. 110, p. 107562, 2021.
- [75] Y. Huo, Z. Xu, H. Moon, S. Bao, A. Assad, T. Moyo, M. Savona, R. Abramson, and B. Landman, "SynSeg-Net: Synthetic Segmentation Without Target Modality Ground Truth," *IEEE Transactions on Medical Imaging*, vol. 38, no. 4, pp. 1016–1025, 2019.
- [76] C. Chen, Q. Dou, H. Chen, J. Qin, and P.-A. Heng, "Synergistic Image and Feature Adaptation: Towards Cross-Modality Domain Adaptation for Medical Image Segmentation," *Proceedings of the AAAI Conference on Artificial Intelligence*, vol. 33, pp. 65–72, 2019.
- [77] N. Karani, E. Erdil, K. Chaitanya, and E. Konukoglu, "Test-time adaptable neural networks for robust medical image segmentation," *Medical Image Analysis*, vol. 68, p. 101907, 2021.
- [78] Y. He, A. Carass, L. Zuo, B. Dewey, and J. Prince, "Autoencoder Based Self-Supervised Test-Time Adaptation for Medical Image Analysis," *Medical Image Analysis*, p. 102136, 2021.
- [79] A. V. Dalca, E. Yu, P. Golland, B. Fischl, M. Sabuncu, and J. Eugenio Iglesias, "Unsupervised Deep Learning for Bayesian Brain MRI Segmentation," in *Medical Image Computing and Computer Assisted Intervention*, 2019, pp. 356–365.
- [80] B. Billot, D. N. Greve, K. Van Leemput, B. Fischl, J. E. Iglesias, and A. Dalca, "A Learning Strategy for Contrast-agnostic MRI Segmentation," in *Medical Imaging with Deep Learning*, 2020, pp. 75–93.
- [81] B. Billot, E. Robinson, A. Dalca, and J. E. Iglesias, "Partial Volume Segmentation of Brain MRI Scans of Any Resolution and Contrast," in *Medical Image Computing and Computer Assisted Intervention*, 2020, pp. 177–187.
- [82] J. E. Iglesias, B. Billot, Y. Balbastre, A. Tabari, J. Conklin, R. Gilberto González, D. C. Alexander, P. Golland, B. L. Edlow, and B. Fischl, "Joint super-resolution and synthesis of 1 mm isotropic MP-RAGE volumes from clinical MRI exams with scans of different orientation, resolution and contrast," *NeuroImage*, vol. 237, 2021.
- [83] V. Arsigny, O. Commowick, X. Pennec, and N. Ayache, "A log-Euclidean framework for statistics on diffeomorphisms," in *Medical Image Computing and Computer Assisted Intervention*, 2006.
- [84] H. Gudbjartsson and S. Patz, "The Rician Distribution of Noisy MRI Data," *Magnetic resonance in medicine*, pp. 910–914, 1995.
- [85] J. Sled and G. Pike, "Understanding intensity non-uniformity in MRI," in *Medical Image Computing and Computer Assisted Intervention*, 1998, pp. 614–622.
- [86] J. Pauly, P. Le Roux, D. Nishimura, and A. Macovski, "Parameter relations for the Shinnar-Le Roux selective excitation pulse design algorithm (NMR imaging)," *IEEE Transactions on Medical Imaging*, vol. 10, no. 1, pp. 53–65, 1991.
- [87] B. Billot, S. Cerri, K. Van Leemput, A. Dalca, and J. E. Iglesias, "Joint Segmentation Of Multiple Sclerosis Lesions And Brain Anatomy In MRI Scans Of Any Contrast And Resolution With CNNs," in *IEEE International Symposium on Biomedical Imaging*, 2021, pp. 1971–1974.
- [88] S. Ioffe and C. Szegedy, "Batch Normalization: Accelerating Deep Network Training by Reducing Internal Covariate Shift," in *International Conference on Machine Learning*, 2015, pp. 448–456.
- [89] D.-A. Clevert, T. Unterthiner, and S. Hochreiter, "Fast and Accurate Deep Network Learning by Exponential Linear Units (ELUs)," *arXiv:1511.07289 [cs]*, 2016.
- [90] D. Kingma and J. Ba, "Adam: A Method for Stochastic Optimization," *arXiv:1412.6980 [cs]*, 2017.
- [91] F. Chollet, "Keras," 2015, <https://keras.io>.
- [92] M. Abadi, P. Barham, J. Chen, Z. Chen, and A. Davis, "Tensorflow: A system for large-scale machine learning," in *Symposium on Operating Systems Design and Implementation*, 2016, pp. 265–283.
- [93] B. Fischl, D. Salat, E. Busa, M. Albert *et al.*, "Whole brain segmentation: automated labeling of neuroanatomical structures in the human brain," *Neuron*, vol. 33, pp. 41–55, 2002.
- [94] D. Van Essen, K. Ugurbil, E. Auerbach, D. Barch, T. Behrens *et al.*, "The Human Connectome Project: A data acquisition perspective," *NeuroImage*, vol. 62, no. 4, pp. 2222–2231, 2012.
- [95] A. Di Martino, C.-G. Yan, Q. Li, E. Denio, F. Castellanos *et al.*, "The Autism Brain Imaging Data Exchange: Towards Large-Scale Evaluation of the Intrinsic Brain Architecture in Autism," *Molecular psychiatry*, vol. 19, no. 6, pp. 659–667, 2014.
- [96] T. A.-. Consortium, "The ADHD-200 Consortium: A Model to Advance the Translational Potential of Neuroimaging in Clinical Neuroscience," *Frontiers in Systems Neuroscience*, vol. 6, 2012.
- [97] A. Holmes, M. Hollinshead, T. O'Keefe, V. Petrov, G. Fariello *et al.*, "Brain Genomics Superstruct Project initial data release with structural, functional, and behavioral measures," *Scientific Data*, vol. 2, no. 1, pp. 1–16, 2015.
- [98] A. Dagley, M. LaPoint, W. Huijbers, T. Hedden, D. McLaren *et al.*, "Harvard Aging Brain Study: dataset and accessibility," *NeuroImage*, vol. 144, pp. 255–258, 2017.
- [99] R. Gollub, J. Shoemaker, M. King, T. White, S. Ehrlich *et al.*, "The MCIC collection: a shared repository of multi-modal, multi-site brain image data from a clinical investigation of schizophrenia," *Neuroinformatics*, vol. 11, no. 3, pp. 367–388, 2013.
- [100] D. Marcus, T. Wang, J. Parker, J. Csernansky, J. Morris, and R. Buckner, "Open Access Series of Imaging Studies: Cross-sectional MRI Data in Young, Middle Aged, Nondemented, and Demented Older Adults," *Journal of cognitive neuroscience*, vol. 19, pp. 498–507, 2007.
- [101] K. Marek, D. Jennings, S. Lasch, A. Siderowf, C. Tanner, T. Simuni *et al.*, "The Parkinson Progression Marker Initiative (PPMI)," *Progress in Neurobiology*, vol. 95, no. 4, pp. 629–635, 2011.
- [102] J. E. Iglesias, R. Insausti, G. Lerma-Usabiaga, M. Bocchetta, K. Van Leemput, and D. Greve, "A probabilistic atlas of the human thalamic nuclei combining ex vivo MRI and histology," *NeuroImage*, vol. 183, pp. 314–326, 2018.
- [103] B. Fischl, D. Salat, A. van der Kouwe, N. Makris, F. Ségonne, B. Quinn, and A. Dale, "Sequence-independent segmentation of magnetic resonance images," *NeuroImage*, vol. 23, pp. 69–84, 2004.
- [104] J. West, J. Fitzpatrick, M. Wang, B. Dawant, C. Maurer, R. Kessler, R. Maciunas *et al.*, "Comparison and Evaluation of Retrospective

- Intermodality Brain Image Registration Techniques," *Journal of Computer Assisted Tomography*, vol. 21, no. 4, pp. 554–568, 1997.
- [105] W. Tae, S. Kim, K. Lee, E. Nam, and K. Kim, "Validation of hippocampal volumes measured using a manual method and two automated methods (FreeSurfer and IBASPM) in chronic major depressive disorder," *Neuroradiology*, vol. 50, no. 7, pp. 569–581, 2008.
  - [106] O. Puonti, K. Van Leemput, G. Saturnino, H. Siebner, K. Madsen, and A. Thielscher, "Accurate and robust whole-head segmentation from magnetic resonance images for individualized head modeling," *NeuroImage*, vol. 219, p. 117044, 2020.
  - [107] S. Farcito, O. Puonti, H. Montanaro, G. Saturnino, J. Nielsen, C. Madsen, H. Siebner, and A. Thielscher, "Accurate anatomical head segmentations: a data set for biomedical simulations," in *Annual International Conference of the IEEE Engineering in Medicine and Biology Society*, 2019, pp. 6118–6123.
  - [108] O. Puonti, J. E. Iglesias, and K. Van Leemput, "Fast and sequence-adaptive whole-brain segmentation using parametric Bayesian modeling," *NeuroImage*, vol. 143, pp. 235–249, 2016.
  - [109] D. Callen, S. Black, F. Gao, C. Caldwell, and J. Szalai, "Beyond the hippocampus: MRI volumetry confirms widespread limbic atrophy in AD," *Neurology*, vol. 57, no. 9, pp. 1669–1674, 2001.
  - [110] M. Chupin, E. G  rardin, R. Cuingnet, C. Boutet, L. Lemieux, S. Le  ricy *et al.*, "Fully automatic hippocampus segmentation and classification in Alzheimer's disease and mild cognitive impairment applied on data from ADNI," *Hippocampus*, vol. 19, no. 6, pp. 579–587, 2009.
  - [111] J. Cohen, *Statistical Power Analysis for the Behavioural Sciences*. Routledge Academic, 1988.



**Axel Thielscher** obtained two PhDs in Biomedical Sciences and Electrical Engineering, both at the University of Ulm (Germany). He is now a Professor of Neurophysics and Neuroimaging at the Technical University of Denmark. His research revolves around providing neuroscience interventional tools to demonstrate the link from brain activity to behaviour, and includes the integration of computational dosimetry methods for brain stimulation.



**Koen Van Leemput** obtained his PhD from the KU Leuven, Belgium, in 2001. He is a faculty member at the Martinos Center for Biomedical Imaging and at the Technical University of Denmark. His research focuses on developing open-source neuroimaging computational models that easily extrapolate to clinical settings, i.e., that can handle pathologies and that work out-of-the-box on data acquired with different scanning hardware, software and protocols.



**Benjamin Billot** holds MSc degrees in electrical engineering (CentralSupélec, France), and biomedical engineering (Imperial College London). He is a third-year PhD candidate at University College London (UCL) at the Centre for Medical Image Computing (CMIC). His thesis focuses on improving the generalisation ability of learning-based methods for analysis of medical images in neuroimaging studies.



**Bruce Fischl** is a Professor of Radiology at the Martinos Center for Biomedical Imaging and an affiliated researcher at MIT. His research involves the development of techniques for cortical surface modelling, thickness measurement, inter-subject registration, whole-brain segmentation and cross-scale imaging. The tools that have resulted from this research have been downloaded over 50,000 times and are in use in labs around the world.



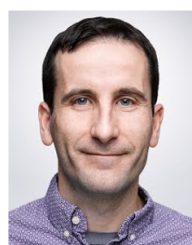
**Douglas N. Greve** obtained his PhD in Cognitive and Neural Systems from Boston University in 1995. He is now an Assistant Professor of Radiology at the Martinos Center for Biomedical Imaging (Massachusetts General Hospital and Harvard Medical School). His research focuses on developing brain image analysis softwares, and he has been one of the core developers of the neuroimaging package FreeSurfer since 1999.



**Adrian V. Dalca** is an assistant professor at Harvard Medical School, Massachusetts General Hospital, and a Research Scientist in CSAIL, MIT. His research focuses on machine learning techniques and probabilistic models for medical image analysis. Driven by clinical questions, he develops core learning algorithms, as well as registration, segmentation and imputation methods aimed at clinical-sourced datasets and broadly applicable in image analysis.



**Oula Puonti** received an MSc degree in theoretical physics from the University of Helsinki, and a PhD in computer science from the Technical University of Denmark. He currently works as postdoctoral researcher at the Danish Research Centre for Magnetic Resonance (DRCMR). His research interests include analysis of human brain structure, biophysical modelling, machine learning, Bayesian modelling, and statistics.



**Juan Eugenio Iglesias** received his PhD in biomedical engineering from University of California Los Angeles. He was a postdoctoral fellow at the Martinos Center for Biomedical Imaging (Massachusetts General Hospital and Harvard Medical School) and the Basque Center for Cognition Brain and Language. He now holds part-time appointments at University College London (sponsored by a European Research Council Starting Grant) and at the Martinos Center.

# SynthSeg: Domain Randomisation for Segmentation of Brain MRI Scans of any Contrast and Resolution

## Supplementary materials

Benjamin Billot, Douglas N. Greve, Oula Puonti, Axel Thielscher, Koen Van Leemput, Bruce Fischl, Adrian V. Dalca, and Juan Eugenio Iglesias

### SUPPLEMENT 1: VALUES OF THE GENERATIVE MODEL HYPERPARAMETERS

TABLE S1

Values of the hyperparameters controlling the generative model. Intensity parameters assume an input in the  $[0, 255]$  interval. Rotations are expressed in degrees, and spatial measures are in millimeters.

Hyperparameter	$a_{rot}$	$b_{rot}$	$a_{sc}$	$b_{sc}$	$a_{sh}$	$b_{sh}$	$a_{tr}$	$b_{tr}$	$b_{nonlin}$	$a_{\mu}$	$b_{\mu}$	$a_{\sigma}$	$b_{\sigma}$	$b_B$	$\sigma_{\gamma}^2$	$r_{targ}$	$b_{res}$	$a_{\alpha}$	$b_{\alpha}$
Value	-15	15	0.85	1.15	-0.012	0.012	-20	20	3	10	240	1	25	0.5	0.4	1	9	0.95	1.15

### SUPPLEMENT 2: LIST OF LABEL VALUES USED DURING TRAINING

TABLE S2

List of the labels used during generation, skull stripping simulation, prediction and evaluation. Different contralateral labels are used for structures marked with <sup>R/L</sup>. Note that the CSF is not always removed when simulating skull stripping.

Label	removed for skull stripping simulation	predicted	evaluated
Background	N/A	yes	no
Cerebral white matter <sup>R/L</sup>	no	yes	yes
Cerebral cortex <sup>R/L</sup>	no	yes	yes
Lateral ventricle <sup>R/L</sup>	no	yes	yes
Inferior Lateral Ventricle <sup>R/L</sup>	no	yes	no
Cerebellar white matter <sup>R/L</sup>	no	yes	yes
Cerebellar grey matter <sup>R/L</sup>	no	yes	yes
Thalamus <sup>R/L</sup>	no	yes	yes
Caudate <sup>R/L</sup>	no	yes	yes
Putamen <sup>R/L</sup>	no	yes	yes
Pallidum <sup>R/L</sup>	no	yes	yes
Third ventricle	no	yes	yes
Fourth ventricle	no	yes	yes
Brainstem	no	yes	yes
Hippocampus <sup>R/L</sup>	no	yes	yes
Amygdala <sup>R/L</sup>	no	yes	yes
Accumbens area <sup>R/L</sup>	no	yes	no
Ventral DC <sup>R/L</sup>	no	yes	no
Cerebral vessels <sup>R/L</sup>	no	no	no
Choroid plexus <sup>R/L</sup>	no	no	no
White matter lesions <sup>R/L</sup>	no	no	no
Cerebro-spinal Fluid (CSF)	yes/no	no	no
Artery	yes	no	no
Vein	yes	no	no
Eyes	yes	no	no
Optic nerve	yes	no	no
Optic chiasm	yes	no	no
Soft tissues	yes	no	no
Rectus muscles	yes	no	no
Mucosa	yes	no	no
Skin	yes	no	no
Cortical bone	yes	no	no
Cancellous bone	yes	no	no

### SUPPLEMENT 3: VERSIONS OF THE TRAINING LABEL MAPS

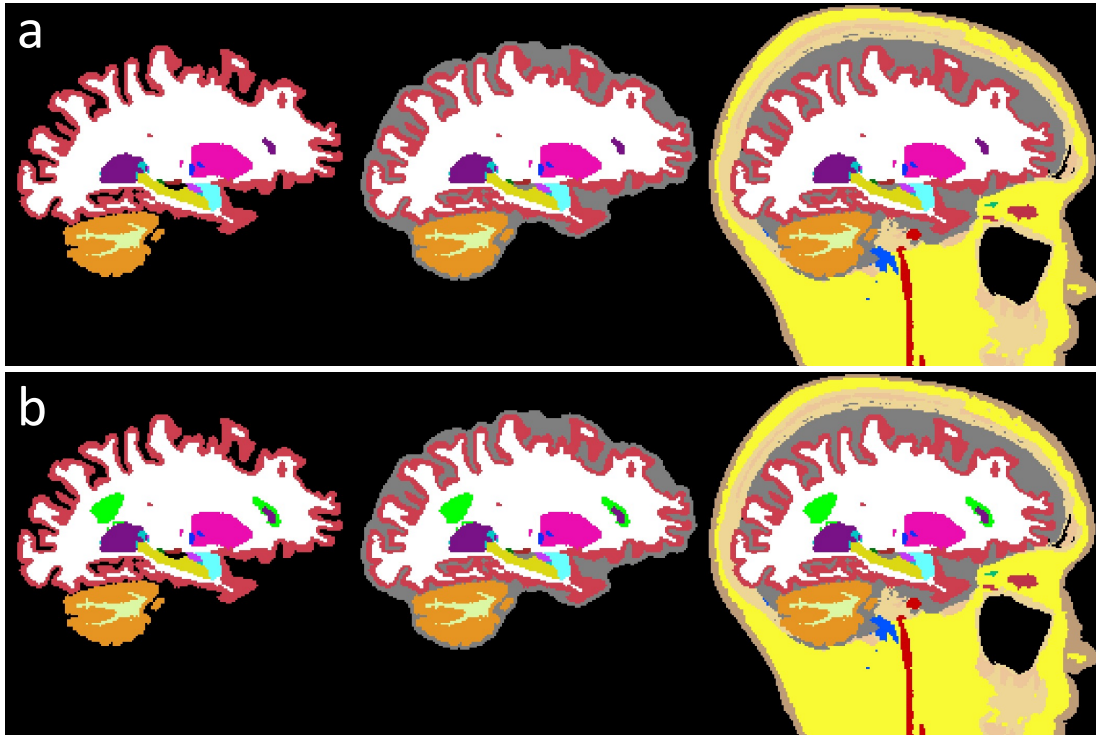


Fig. S1. Example of all versions of the training label maps: (a) without, and (b) with lesion labels (bright green). Using these different versions builds robustness to white matter lesions and to (possibly imperfect) skull stripping. The added extra-cerebral labels (left) are obtained with a Bayesian segmentation approach [106], for which we only had access to the atlas (not to the manual delineations used for its construction [107]).

### SUPPLEMENT 4: MODIFICATIONS TO THE TTA FRAMEWORK

The TTA approach presented in this paper is based on the work of Karani et al. [1]. Importantly we make the following changes with the original paper, which we find to substantially improve the results on the validation set. First, we increase the number of layers used for the image normaliser to improve its learning capacity, especially for large domain gaps (e.g., cross-modality adaptation). Second, we rigidly register the atlas used for fine-tuning to every test scan, and we increase its usage throughout the adaptation to target space by decreasing the  $\beta$  threshold to 0.4 [1].

### SUPPLEMENT 5: NUMBER OF RETRAINING FOR EACH VALUE OF $N$

TABLE S3

Number of label maps and associated retrainings used to assess performance against the amount of training subjects.

Number of training segmentations	1	5	10	15	20
Number of retrainings	8	5	4	3	2

[1] N. Karani, E. Erdil, K. Chaitanya, and E. Konukoglu, "Test-time adaptable neural networks for robust medical image segmentation," *Medical Image Analysis*, vol. 68, p. 101907, 2021.